HYPERON-ANTIHYPERON PRODUCTION IN $\bar{P}P$ INTERACTIONS AT 2.4 AND 2.9 GeV/c

by

Terry LeRoy Schalk

A Dissertation Submitted to the
Graduate Faculty in Partial Fulfillment of
The Requirements for the Degree of
DOCTOR OF PHILOSOPHY

Major Subject: High Energy Physics

Approved:

Signature was redacted for privacy.

In Charge of Major Work

Signature was redacted for privacy.

Head of Major Department

Signature was redacted for privacy.

Dean of Graduate College

Iowa State University
Of Science and Technology
Ames, Iowa

1969

TABLE OF CONTENTS

		Page
I.	INTRODUCTION	1
II.	EXPERIMENT	3
	A. Film Exposure	3
	B. Scanning	4
	C. Measuring	10
	D. Beam Properties and Event Identification	15
III.	CROSS-SECTIONS	20
IV.	TWO-BODY FINAL STATES	26
	A. Neutral	26
	B. Charged 2-body Final States	44
	C. Comparison with SU_3	48
V.	3 AND 4 BODY FINAL STATES	50
VI.	CONCLUSIONS	57
VII.	BIBLIOGRAPHY	59
VIII.	ACKNOWLEDGMENTS	61
IX.	APPENDIX	62

I. INTRODUCTION

In any high energy bubble chamber experiment, it is possible to study all charged particle final states (with or without one unobserved neutral particle) produced by the given interaction. It is also possible to study those neutral final states where the neutrals are observed to decay to observed charged tracks or to interact yielding observed tracks. This is a study of those final states in antiproton-proton ($\bar{P}P$) interactions in which antihyperons and hyperons are produced. (A hyperon is a particle with baryon number = 1 and strangeness = -1, -2, or -3)

A total of 150,000 pictures were taken at each of two momenta (2.4 and 2.9 GeV/c) in the BNL 31-inch hydrogen bubble chamber yielding an antiproton path length of $.62 \times 10^6$ meters at each momentum. The production of antihyperons and hyperons is only a small percentage ($\lesssim 2\%$) of the total $\bar{p}$ - p cross-section at these momenta, thus requiring a large number of pictures for such a study.

The purpose of the experiment was to study the production of all strangeness -1 and -2 hyperons and their anti-particles; their cross-sections, angular distributions, production processes, and symmetry properties.

In the 2-body final states $\Lambda\bar{\Lambda}$ and $\Lambda\overline{\Sigma^o}$ + c.c.[1], the hyperons (anti-hyperons) observed were produced very strongly forward (backward). That is, the hyperons were strongly correlated with the target proton direction and the antihyperons with the $\bar{P}$ beam direction in the center of mass system. This peripheral nature of the interaction has been observed in

---

[1] The notation +c.c. is a contraction for "plus charge conjugate", for example $\Lambda\overline{\Sigma^o}$ + c.c. means $\Lambda\overline{\Sigma^o}$ plus $\bar{\Lambda}\Sigma^o$.

similar exposures at 2.2, 2.5, 2.7, 3.0, 3.25, 3.6, 3.69, 3.7, 4.0, 5.7, and 6.9 GeV/c (1-8), becoming more pronounced at higher beam momenta.

The discussion is broken into six sections: the experimental procedures are detailed in Section II, and the cross-sections discussed in Section III. Section IV is devoted to the 2-body final states (both neutral and charged). Included in this section is a discussion of the density matrix elements for the reaction, $\bar{p}\, p \rightarrow \bar{\Lambda}\, \Lambda$, and a comparison of the 2-body cross-sections with SU_3 predictions. The three $\Xi\, \bar{\Xi}$ events found at 2.9 GeV/c are also discussed in this section. The three and four body final states are discussed in Section V. Some indication of $\Sigma(1385)$ production was observed in the $\bar{\Lambda}\, \Sigma^+\, \pi^-$ + c.c. final states and in the final state $\Lambda\, \bar{\Lambda}\, \pi^o$. A search for evidence of resonance production was not carried out in the four-body final states due to the small magnitude of these cross-sections. This small cross section results in very few events in these channels at these energies. Section VI summarizes the experiment.

II. EXPERIMENT

A. Film Exposure

The two beam momenta were primarily selected for a study of the reaction $\bar{P}P \rightarrow \bar{\Delta}^{++} \Delta^{++}$ (9) near threshold, which used 60,000 pictures at 2.4 GeV/c and 40,000 pictures at 2.9 GeV/c. These first 100,000 pictures were taken in June of 1967. In addition, another 200,000 pictures, used only for strange particle production, were then taken in September of 1967.[2]

The antiprotons were obtained by striking an internal target with the proton beam of the Brookhaven National Laboratory Alternating Gradient Synchrotron (AGS). All negative secondaries within a certain angular region were then accepted as input to a series of magnets and electrostatic separators which selected out a specified momentum interval and also separated the $\bar{P}$'s, K's, and π's. This separated $\bar{P}$ beam was then incident upon the 31-inch Hydrogen Bubble Chamber. A Čerenkov counter[3] was set to detect π's, μ's, and K's and used to give an upper limit to the beam contamination. This counter gave only an upper limit to the contamination as it also counted those off-momentum particles resulting from interactions along the beam line. This upper limit was $< 1\%$ for both beam momenta in run 1 and $< 1\%$ and $< 2.5\%$ for the 2.4 and 2.9 GeV/c momenta respectively in run 2.

The second bubble chamber run made in September 1967 used the same

---

[2] These two exposures will be referred to as run 1 and run 2.

[3] A Čerenkov counter is sensitive to the velocity of the traversing particle. Thus, placed in a beam of particles with a known momentum, it can be used to determine the indentity of the particle.

beam line and 31-inch BNL chamber yielding a total of 300,000 pictures split equally between 2.4 GeV/c and 2.9 GeV/c.

The exact value of the beam momentum for the first exposure was determined from known 4-constraint[4] $\bar{p}\,p \rightarrow \bar{p}\,p\,\pi^+\,\pi^-$ events by ignoring the beam momentum and reprocessing them with the beam momentum unknown. This yielded beam momenta of $2.885 \pm .080$ GeV/c and $2.375 \pm .075$ GeV/c. To guarantee that run 2 had a momentum consistent with run 1, a sample of elastic $\bar{P}P$ interactions was measured from the second run. These were then processed with the beam momentum again treated as unknown (589 events were measured at the lower momentum and 720 at the higher momentum). These yielded values of $2.875 \pm .080$ and $2.355 \pm .075$ GeV/c for the beam momenta in run 2. For brevity these beam momenta will be referred to as 2.9 and 2.4 GeV/c.

A sample of μ's (from $\pi\mu e$ decays) were also measured from both the first and second run to determine the density of the hydrogen in each run. These yielded densities of $.0658 \pm .0005$ and $.0658 \pm .0015$ g/cm^3 in run 1 and run 2 respectively.

B. Scanning

The film was scanned to find those frames in which visible $\bar{P}$-P interactions took place. Only those interactions which produced charged particles were visible in the bubble chamber. The strange particle interactions were characterized by the production of particles whose lifetimes are typical of the weak interactions ($1\text{-}3 \times 10^{-10}$ seconds) and as such

[4] A 4-constraint fit is a fit to the event of a specified set of particle masses using the 4-constraint conditions of conservation of energy and vector momentum (10).

usually decayed in the chamber. The neutral strange particles produced decayed to neutral or to charged non-strange particles. It was the charged particle decay mode, seen as two charged tracks forming a "V", which was observed in the bubble chamber. A charged strange particle decay appeared as a "kink" in a track where the track suddenly changed direction.

Thus, the strange particle topology was that with one or more visible decay tracks coming from a production vertex and/or one or more vees appearing downstream (relative to the beam direction).

A topology with two outgoing tracks at the production vertex, one of which decayed, and having an associated vee, is sketched below:

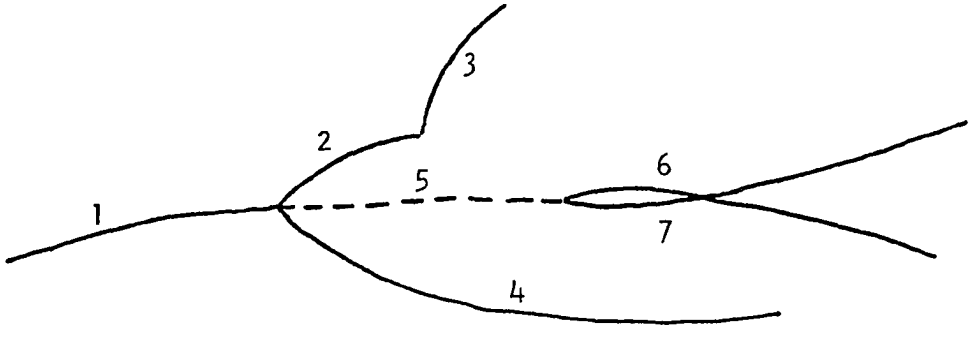

Track 1 is the incoming $\bar{P}$ beam track. Track 2 decays into track 3 and at least one unseen neutral particle. Track 5 is an unseen neutral strange particle which decays into tracks 6 and 7 forming a vee.

As the film was scanned, the roll, frame, topology (defined by ℓ prongs-m decays-n vees), and a rough location within the frame was recorded. This identification information was used to find the event both when it was measured and when it was later checked for consistency with a specified mass hypothesis.

The results of the first scan are displayed in Table I and II, and the scanning efficiency for each topology from a section of the 2.9 GeV/c data

Table I. Summary of scan 1 - 2.4 GeV/c

Types	First 31 Rolls of Film No. Events	Next 45 Rolls No. Events
0 prong	2,703	--
0 prong 1 Vee	186	301
0 prong 2 Vee	70	129
0 prong 3 Vee	--	4
0 prong 4 Vee	1	--
1 prong	9	--
1 prong 1 Vee	1	8
2 prong	46,446	--
2 prong 1 Vee	873	1,360
2 prong 2 Vee	81	166
2 prong 3 Vee	1	2
2 prong 1 decay	188	153
2 prong 2 decay	24	36
2 prong 1 Vee 1 decay	13	41
2 prong 2 Vee 1 decay	1	2
3 prong	61	--
3 prong 1 Vee	--	6
3 prong 2 Vee	--	1
3 prong ! decay	2	2
4 prong	26,135	--
4 prong 1 Vee	412	601
4 prong 2 Vee	15	27
4 prong 1 decay	329	98

Table I. (Continued)

Types	First 31 Rolls of Film No. Events	Next 45 Rolls No. Events
4 prong 2 decay	3	14
4 prong 1 Vee 1 decay	14	33
4 prong 1 Vee 2 decay	--	1
4 prong 2 Vee 1 decay	--	1
5 prong	42	--
5 prong 1 Vee	4	2
6 prong	5,910	--
6 prong 1 Vee	40	59
6 prong 2 Vee	2	--
6 prong 1 decay	64	--
6 prong 2 decay	1	--
6 prong 1 Vee 1 decay	3	1
7 prong	4	--
8 prong	168	--
8 prong 1 Vee	2	5
8 prong 1 decay	3	--

Table II. Summary of scan 1 - 2.9 GeV/c

Types	First 21 Rolls of Film No. Events	Next 55 Rolls No. Events
0 prong	1,492	--
0 prong 1 Vee	142	413
0 prong 2 Vee	57	165
0 prong 3 Vee	--	4
1 prong 1 Vee	--	5
1 prong 2 Vee	--	2
1 prong 1 decay	--	1
2 prong	26,469	--
2 prong 1 Vee	454	1,270
2 prong 2 Vee	68	169
2 prong 3 Vee	--	7
2 prong 1 decay	136	286
2 prong 2 decay	12	52
2 prong 1 Vee 1 decay	16	64
2 prong 1 Vee 2 decay	--	2
2 prong 2 Vee 1 decay	--	1
2 prong 2 Vee 2 decay	--	2
3 prong	25	--
3 prong 1 Vee	--	4
4 prong	15,333	--
4 prong 1 Vee	291	726
4 prong 2 Vee	8	45
4 prong 1 decay	188	--

Table II. (Continued)

Types	First 21 Rolls of Film No. Events	Next 55 Rolls No. Events
4 prong 2 decay	1	6
4 prong 1 Vee 1 decay	1	26
4 prong 1 Vee 2 decay	--	1
5 prong	23	--
5 prong 1 decay	2	--
6 prong	3,923	--
6 prong 1 Vee	18	37
6 prong 2 Vee	--	2
6 prong 1 decay	54	--
6 prong 2 decay	1	--
6 prong 1 Vee 1 decay	--	3
7 prong	3	--
8 prong	143	--
8 prong 1 Vee	1	--
8 prong 2 Vee	--	1
8 prong 1 decay	3	--

given in Table III. The combined efficiency for both scans, averaged over all topologies, was 94% at 2.9 GeV/c and 93% at 2.4 GeV/c. A count of all beam tracks was made every tenth frame in one scan to determine the total number of antiprotons in the experiment. This gave a total count of 1.29 x 10^6 $\bar{P}$'s at each momentum.

C. Measuring

All strange particle topologies in the first run (except the 2P - 1V topology) were measured on conventional, manual measuring machines. Before run 2 was measured, these machines were put on line to an ASI 6050 computer. A locally written monitor called KUBER (11) made the use of this on-line system very convenient. It allowed the use of FORTRAN-like controlling routines, on-line reconstruction (local version of HGEOM) and on-line kinematic fitting(GUTS)(10, 12). This on-line system enabled one to know not only that each event was well measured but also the identity and association of each vee measured. Thus, this system greatly reduced the bookkeeping problems inherent in an experiment of this kind.

Since gamma rays which had converted to e+e- pairs also appeared in a picture as a vee, these events would be confused with strange particle events and had to be eliminated. These "vees" had small effective[5] masses

---

[5] The effective mass of N (in this case 2) particles is defined by

$$M_{eff}^2 = \sum_{i=1}^{N} E_i^2 - \left(\sum_{i=1}^{N} \vec{P}_i\right)^2 = \sum_i E_i^2 - \left(\sum_i \vec{P}_i\right)\cdot\left(\sum_i \vec{P}_i\right)$$

where $E_i^2 = P_i^2 + M_i^2$ the energy of particle i with momentum $\vec{P}_i$ and mass m_i. Notice that since the mass of an electron is so small (.511 MeV) compared with the momentum resolution (~1 MeV/c), that $M_{eff} \approx 0$ for a real e+e- pair with small opening angle.

Table III. Efficiency scan of 55 rolls - 2.9 GeV/c

Types	Scan 1 (%)	Scan 2 (%)	
0 prong 1 Vee	69	71	
0 prong 2 Vee	74	80	
0 prong 3 Vee	0	0	(small no.)
1 prong 1 Vee	56	56	
1 prong 2 Vee	0	0	(small no.)
2 prong 1 Vee	73	71	
2 prong 2 Vee	79	77	
2 prong 3 Vee	56	78	
2 prong 1 decay	63	67	
2 prong 2 decay	79	73	
2 prong 1 decay 1 Vee	75	70	
2 prong 2 decay 1 Vee	0	0	(small no.)
2 prong 2 decay 2 Vee	0	0	(small no.)
2 prong 1 decay 2 Vee	0	0	(small no.)
3 prong 1 Vee			
4 prong 1 Vee	70	71	
4 prong 2 Vee	70	71	
4 prong 2 decay	0	0	(small no.)
4 prong 1 decay 1 Vee	59	74	
4 prong 2 decay 1 Vee	0	0	(small no.)
6 prong 1 Vee	68	50	
6 prong 2 Vee	0	0	(small no.)
8 prong 1 Vee	0	0	(small no.)
8 prong 2 Vee	0	0	(small no.)
All Vees	75	74	
Overall Efficiency	71	71	

($\sim$0 MeV) and very small opening angles compared with real strange particle vees. To determine a method for detecting e^+e^- pairs, a plot of the vee opening angle versus the mass of the vee was examined. Figure 1 shows a sample of vees from the 4-prong 1-vee topology measured off-line where the e+e- pairs were not eliminated at measurement time. The events clustered in the lower left corner of the plot were identified as e+e- pairs. Using this plot all "vees" with mass less than 100 MeV and opening angle less than 7 degrees were classified as e+e- pairs and deleted from the sample of vee events.

Figure 2 shows a flow chart of the program written to control the on-line measurement of vee events. It allowed the measurer to attempt the association of a vee with any likely production vertex as well as forcing her to remeasure the vee if the kinematic fitting routines had any trouble with the fit. Thus, each event had to satisfy the following conditions before the reconstruction and raw data records were written on tape:

1. All identification information as set up by the scanners was correct.
2. All tracks were measured correctly, where "correctly" meant that angle errors were $<3/4^o$ and $\Delta p/p$ <20% for all tracks with length $\geq$ 1 inch.
3. The vee had been identified as a K^o_1, Λ^o or $\overline{\Lambda^o}$, and was not an e+e- pair.
4. The kinematic and reconstruction programs had no trouble in fitting the event.
5. The vee was associated with the correct production vertex.

These reconstruction tape records were then reprocessed with GUTS in an off-line mode.

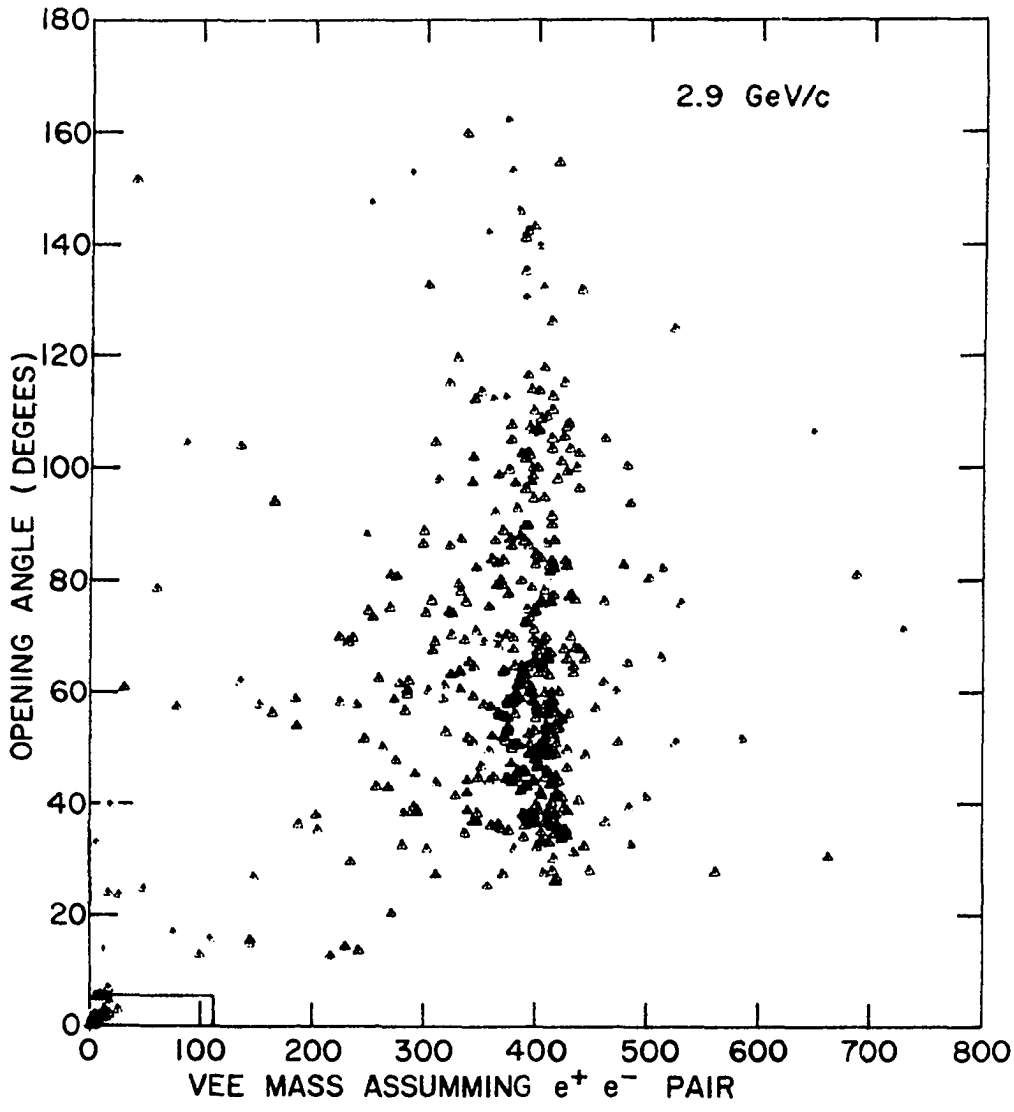

Figure 1. "Vee" opening angle versus the effective mass of the "Vee" where both tracks are assumed to have the mass of an electron.

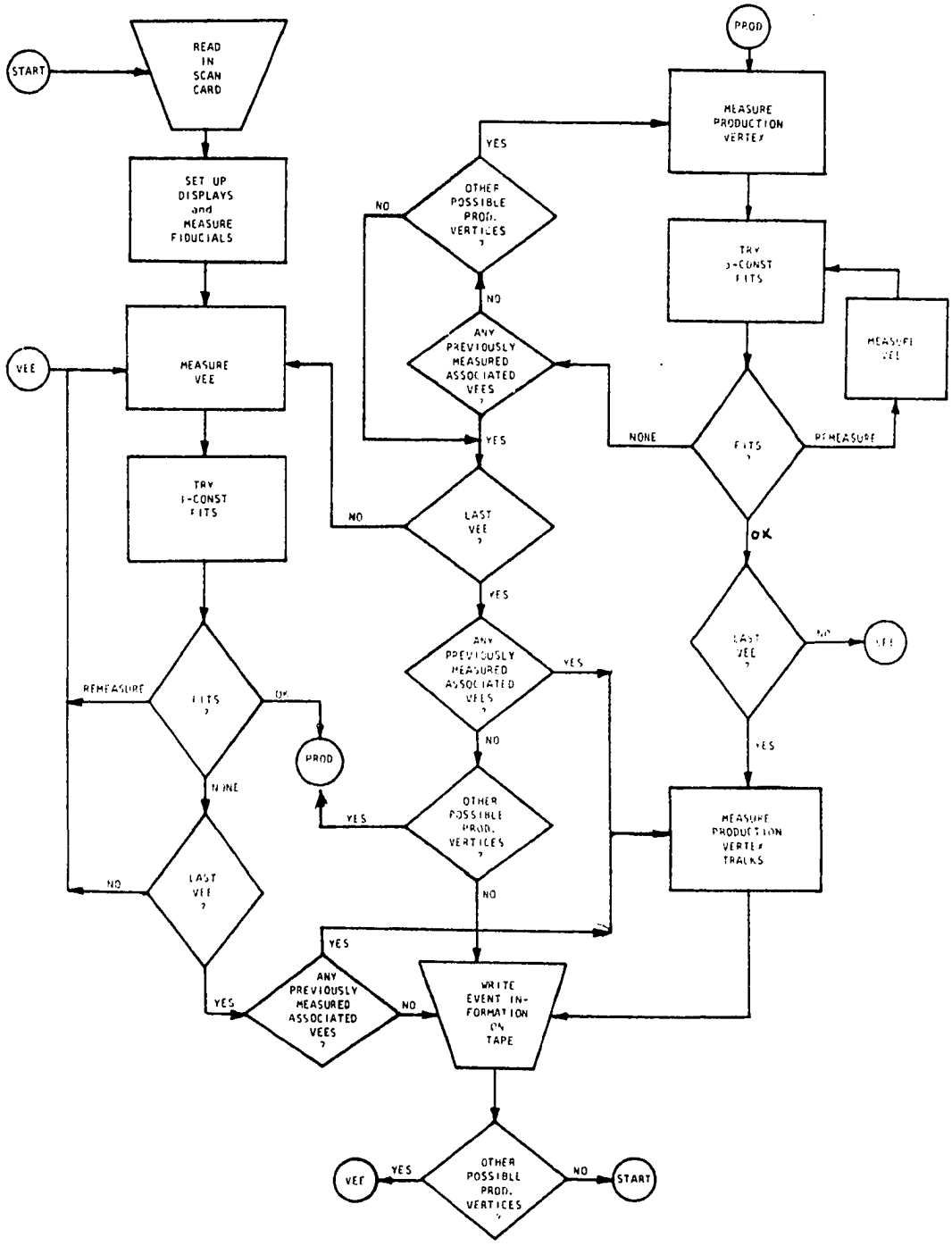

Figure 2. Flow chart for the control program which monitored the on-line measuring

D. Beam Properties and Event Identification

Azimuth and dip angle restriction were made on all beam tracks to insure that no tracks from secondary interactions were classified as beam tracks. The beam azimuth vs. the x position of the production vertex and a histogram of the dip angle for all measured events are shown in Figure 3 for the 2.9 GeV/c data. From these plots (and similar ones at 2.4 GeV/c) the following criteria was used to define good beam tracks

2.9 GeV/c
$$\begin{cases} \text{Azimuth (degrees)} = -.358\ X\ \text{(inches)} + 2.35^{\circ} \pm 1.65^{\circ} \\ \text{Dip (degrees)} = 0^{\circ} \pm 4^{\circ} \end{cases}$$

2.4 GeV/c
$$\begin{cases} \text{Azimuth (degrees)} = -.4X\ \text{(inches)} + 1.9^{\circ} \pm 3.8^{\circ} \\ \text{Dip (degrees)} = 0^{\circ} \pm 4^{\circ} \end{cases}$$

To insure that sufficient track length could be measured, on all tracks in the event, a "fiducial volume" less than the actual volume of the chamber was established. Events whose vertices lie outside this fiducial volume would be expected to have tracks with unacceptably high momentum errors (Δp) and therefore were not used in the experiment. Those events falling outside the fiducial volume were eliminated from the data sample after the events were measured so that this fiducial volume restriction could be applied accurately.

To establish a fiducial volume, plots of $\Delta p/p$ for both vee tracks versus the position of the vee vertex were made. Figure 4 is one such plot from the 2.9 GeV/c data.

Using these plots, a fiducial volume for the vee vertex position (as listed below) was established for use with the production vertex fiducial volume also listed below:

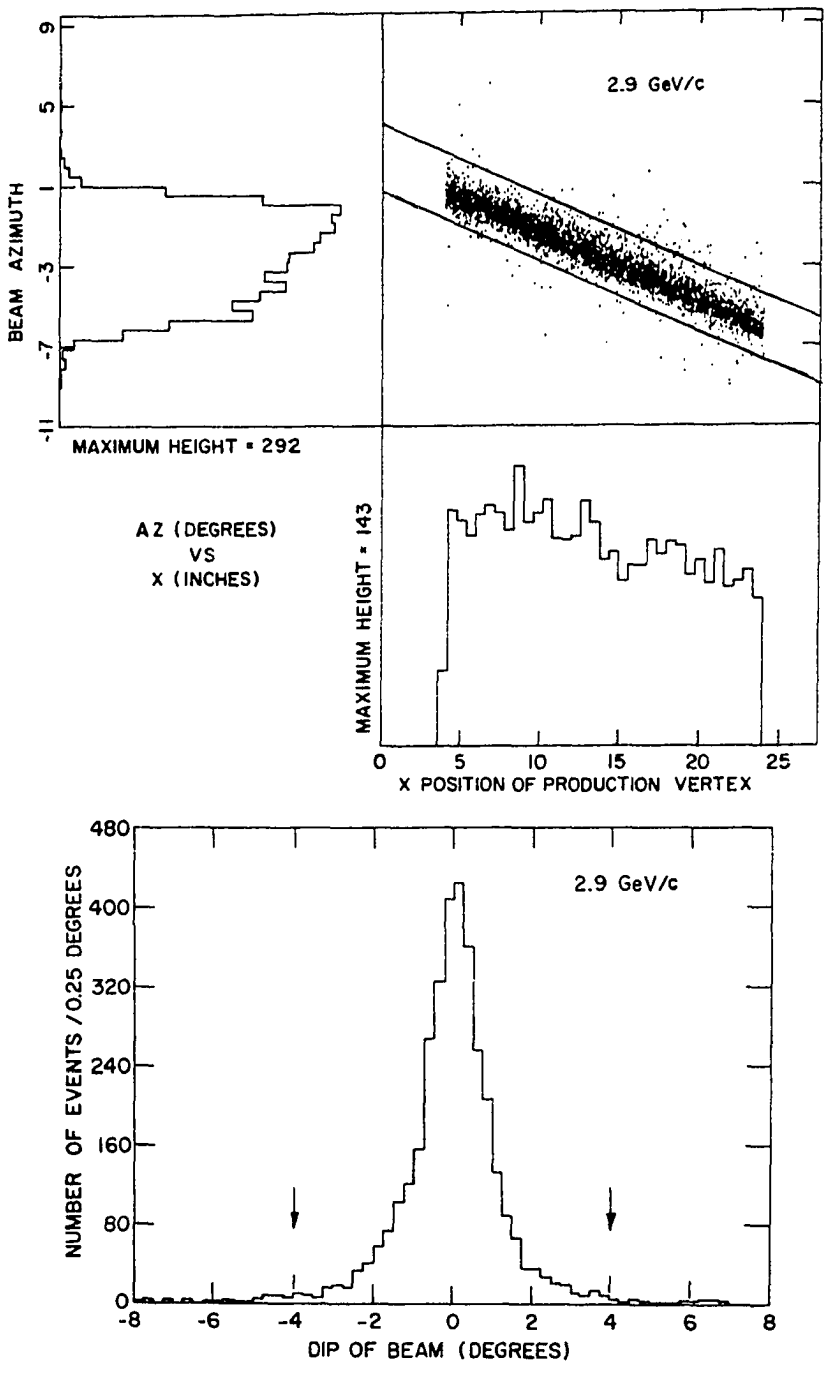

Fig. 3. Azimuth and dip angles of the incident $\bar{p}$ beam as a function of chamber length traversed by $\bar{p}$ before interaction

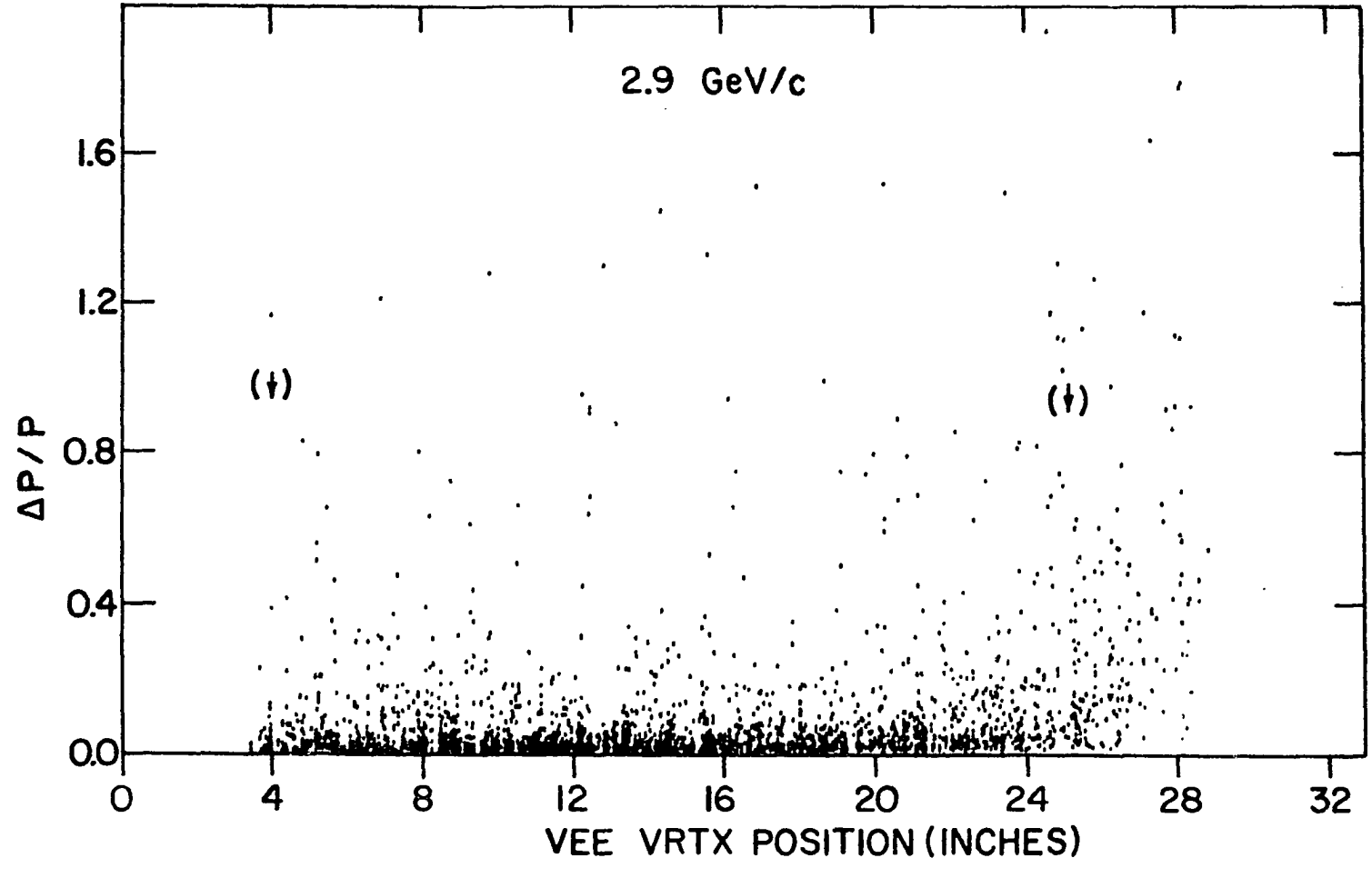

Figure 4. Δp/p for both tracks of the vee versus the vertex position of the vee

Vee Fiducial Volume (in inches)	Production Fiducial Volume (in inches)
$4 \leq X \leq 25$	$4 \leq X \leq 24$
$2 \leq Y \leq 8$	$2.5 \leq Y \leq 8$
$3.5 \leq Z \leq 11$	$5 \leq Z \leq 10$

The fitting program (GUTS) which tried all allowed mass assignments to the measured tracks, did not always produce unambiguous fits to one particular mass assignment. Those events which had GUTS fits ambiguous between two or more final states were classified by either using a missing mass criteron (See Section IV) or by an ionization[6] consistency check. Two major ambiguities remained. Some vees had acceptable fits to both K^o_1 and $\overline{\Lambda^o}$ and could not be distinguished by examining the bubble density of the track, due to the existence of at least one high momentum track. To resolve this ambiguity the angular distribution of the π^+ in the rest frame of the K^o_1 or $\overline{\Lambda^o}$ was examined. This distribution in cos θ_{cm} should be isotopic for a real K^o_1 or $\overline{\Lambda^o}$. The distribution was flat for the unique K^o_1's, strongly peaked forward for ambiguous K^o_1's and non-isotropic for both the unique and ambiguous $\overline{\Lambda^o}$'s. Adding the ambiguous $\overline{\Lambda^o}$'s to the unique sample resulted in the expected flat distribution. Thus, all ambiguous vees were accepted as $\overline{\Lambda^o}$'s. It is estimated that at most a 7% contamination was added to the $\overline{\Lambda^o}$ sample by this procedure.

The second major ambiguity was in the 2-prong 2-decay topology where the final states $\Sigma^+\overline{\Sigma^+}$ and $\Sigma^-\overline{\Sigma^-}$ were often indistinguishable. The reason for this ambiguity is that there is only a 8 MeV mass difference between the Σ^+

[6] The bubble density for tracks in a bubble chamber is $\propto 1/\beta^2$ where $\beta = v/c$. Thus, particles with different masses produce different bubble densities in a given momentum track.

and Σ^-. The only way to distinguish these two final states is to observe the proton decay mode of the Σ^+ (or $\bar{p}$ decay of the $\overline{\Sigma^+}$). A Σ^+ decays 50% to $p\pi^o$ and 50% to π^+N and a Σ^- decay 100% to π^-N(13), so 25% of the $\Sigma^+\overline{\Sigma^+}$ events were necessarily ambiguous with $\Sigma^-\overline{\Sigma^-}$ events. There was another complicating factor in this final state in that these events are also peripherally produced. The $\overline{\Sigma^+}$ produced at small scattering angles with respect to the incident $\bar{p}$ direction in the center of mass, appeared in the laboratory with high momentum. When these high momentum $\bar{\Sigma}$'s decay to $\bar{p}\ \pi^o$, the antiproton is closely aligned with the direction of the $\bar{\Sigma}$ producing either no visible kink in the track or only a very small angle kink which was very easy for the scanners to miss.[7] It is estimated that ~25 % of the $\Sigma\ \bar{\Sigma}$ events were not found for this reason.

---

[7] The $\bar{p}$ appearing from the decay of a $\overline{\Sigma^+}$ produced at 30^o in the center of mass appeared on the film having an angle $< 8^o$ with respect to the $\bar{\Sigma}^+$ direction.

III. CROSS-SECTIONS

The cross-section is defined as:

$$\sigma = \frac{\text{number of interactions/atom}}{\text{incident flux/cm}^2}$$

$$\sigma = \frac{M}{2N_a\rho_{H_2}} * \frac{N}{eL}$$

where $M = 2.016$ gm/mole — Molecular weight of H_2

$N_a = 6.023 \times 10^{23}$ — Avagadro's number

$\rho_{H_2} = .0658$ gm/cm^3 — Density of liquid H_2

N = Number of interactions (weighted)

e = Scan efficiency (given in Section IIB)

yielding $\sigma = 25.42 * \frac{N}{eL}$ (μ barns)

An appreciable fraction of the strange particles produced in the experiment were not detected in the bubble chamber. This was due to one or more of the following reasons:

1. They decayed via a neutral decay mode.
2. They decayed too close to the production vertex to be detected.
3. They decayed outside the bubble chamber (or outside the fiducial volume).
4. The charged strange particles had a projected decay angle on the film too small to be detected.

To correct for this the number of observed interactions in these final states must be weighted by the probability of observing the events.

In order to evaluate this probability, minimum track length limits (1/4 inch for vees and 1/5 inch for charge decays) and projected

charged particle decay angle limits (4^{o}) were established. Events satisfying these decay limits (and the fiducial volume restrictions mentioned earlier) were then weighted by the reciprocal of the detection probability for that particular event. The total number of events for a particular final state was then calculated to be:

$$N = 1/e \left[\sum_i W_i \pm \left(\sum_i W_i^2\right)^{1/2}\right]$$

where W_i is the weight of the ith event. For the Λ and $\bar{\Lambda}$'s observed in the experiment, these weights ranged from 1.61 to 3.85[8] with an average weight of 1.91.

The detection probability P_i for a single neutral hyperon is given by P_i = BR * P (decay), where BR is the branching ratio into charged decay products and P (decay) the probability of decay in the fiducial volume but beyond the minimum track length restriction.

P (decay) is defined to be:

$$P \text{ (decay)} = e^{-t_o/\tau} - e^{-t_{max}/\tau}$$

τ is the mean life of the particle in its rest frame; t_o and t_{max} are the minimum and maximum proper times corresponding to the minimum and maximum times consistent with observation of the decay.

$$t_o = m\, L_o/pc$$

$$t_{max} = m\, L_{max}/pc$$

---

[8]There were two $\bar{\Lambda}^{o}$'s at 2.9 GeV/c with weights greater than 3.85, one with a weight of 4.48 and one with a weight of 6.62.

with m = rest mass of the decaying particle in MeV/c^2

p = laboratory momentum of the decaying particle in MeV/c

L_o = minimum length cut off (in cm.)

L_{max} = maximum path length in the fiducial volume for the event (in cm.)

Since all final states considered involved two strange particles (with probability of detection P_1 and P_2), the total probability of seeing each event with either one or both decays visible was $P_1P_2 + P_1(1-P_2) + P_2(1-P_1)$.

The total $\bar{P}$ path length (L) was calculated as follows: The beam tracks were counted every 10th frame and an average number computed for each roll. This average was then multiplied by the total number of usable frames on that roll.

One must also consider the attenuation of the beam due to interactions. Estimating that one interaction per foot of hydrogen is equivalent to a cross-section of one barn and estimating the average $\bar{P}P$ total cross-section for both momenta to be 79 mb (14) gives 79 interactions in 1,000 feet of hydrogen or 13 interactions per 100 traversals of the fiducial volume. Estimating these interactions to occur on the average 1/2 way across the chamber gives a decrease in the actual path length of (13*1/2) in 100 or a factor of .935. Then the total path length is given by L = .935 * 50.4 * N cm. where N is the total number of beam tracks scanned. Numerical values for the path length and scanning efficiency are given below.

	2.4 GeV/c	2.9 GeV/c
Total number of beam tracks	1.288×10^6	1.282×10^6
Total path length in fiducial volume	60.7×10^6 cm.	60.4×10^6 cm.
Scanning efficiency	93 ± 1%	94% ± 1%

Using the above values gives $\sigma/N(\mu$ barns/event) $= .450 \pm .006$ at 2.4 and $\sigma/N(\mu$ barns/event) $= .448 \pm .006$ at 2.9 GeV/c.

The cross-sections for all hyperon-antihyperon final states are shown in Table IV[9] with the energy dependence of the $\sigma(\Lambda\bar{\Lambda})$ and $\sigma(\Lambda\bar{\Sigma}^{o} + \text{c.c.})$ shown in Figure 5.

---

[9] Events were classified as $\Lambda\ \bar{\Lambda}\ X^{o}$ which had MM > 1250 and which had no acceptable $\Lambda\ \bar{\Lambda}\ \pi^{o}$ fits.

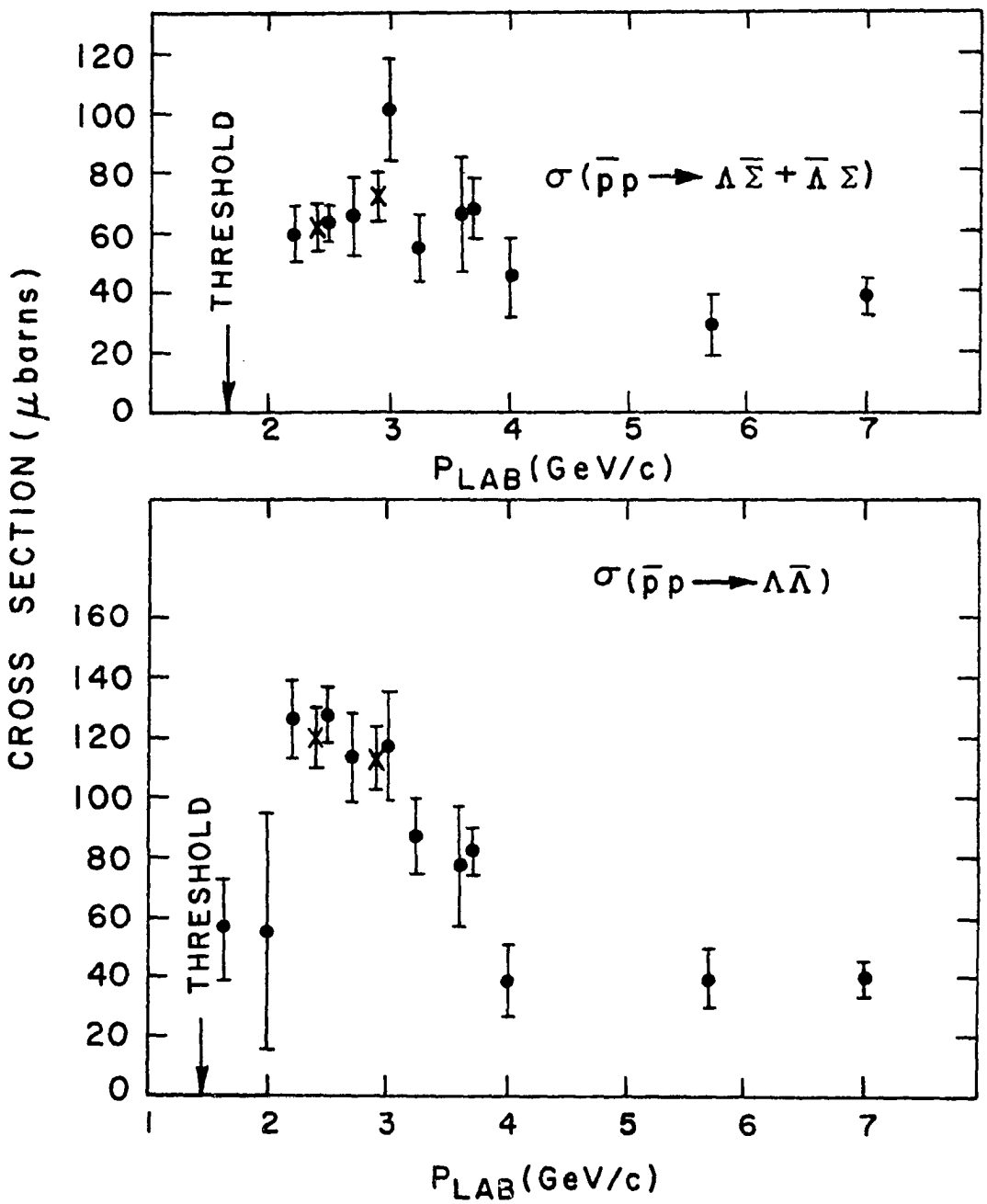

Fig. 5. $\bar{p}p \to \bar{\Lambda}\Lambda$ and $\bar{p}p \to \Lambda\,\overline{\Sigma^0}$ + c.c. cross sections as a function of incident $\bar{p}$ beam momentum

Table IV. Cross-sections for all hyperon-antihyperon final states

Final State	Events observed 2.4	Events observed 2.9	$\sigma(\mu$ barns) 2.4	$\sigma(\mu$ barns) 2.9
$\Lambda\bar{\Lambda}$	139	130	120 ± 11	113 ± 10
$\Lambda\bar{\Sigma}^{o}$ + c.c.	74	80	61 ± 7	71 ± 8
$\Sigma^{\pm}\bar{\Sigma}^{\pm}$	56	51	47 ± 8	43 ± 8
$\Sigma^{o}\bar{\Sigma}^{o}$	-	-	< 27	< 26
$\Xi^{-}\bar{\Xi}^{-}$	-	3	-	4 ± 2
$\Xi^{o}\bar{\Xi}^{o}$	-	-	-	-
$\Lambda\bar{\Lambda}\pi^{o}$	9	46	15 ± 5	78 ± 18
$\Lambda\bar{\Lambda}X^{o}$	1	9	1.6 ± 1.6	15 ± 9
$\Sigma^{\pm}\bar{\Sigma}^{\pm}\pi^{o}$	-	3	-	2.5 ± 1.5
$\Sigma^{\pm}\bar{\Sigma}^{o}\pi^{\mp}$ + c.c.	-	7	-	8.2 ± 3.1
$\Sigma^{\pm}\bar{\Lambda}\pi^{-}$ + c.c.	3	31	3.2 ± 2.0	36 ± 6
$\Sigma^{-}\bar{\Lambda}\pi^{+}$ + c.c.	5	21	5 ± 2.5	24.5 ± 5
$\Sigma^{\pm}\bar{\Lambda}\pi^{\pm}\pi^{o}$ + c.c.	-	3	-	3.5 ± 2
$\Lambda\bar{\Lambda}\pi^{+}\pi^{-}$	0	5	$< .8$	4.3 ± 2.2
$\Lambda\bar{\Sigma}^{o}\pi^{+}\pi^{-}$ + c.c.	0	3	$< .8$	2.6 ± 1.1
$\Lambda K^{o}_{1}\bar{N}$ + c.c.	0	6	$< .8$	7.7 ± 4.0
$\Lambda K^{+}\bar{p}$ + c.c.	1	5	$.8 \pm .8$	5 ± 3.5

IV. TWO-BODY FINAL STATES

A. Neutral

The neutral 2-body strange particle final states were:

1. $\bar{p} + p \rightarrow \bar{\Lambda} + \Lambda$

2. $\rightarrow \Lambda + \bar{\Sigma}^{o}$, $\bar{\Sigma}^{o} \hookrightarrow \bar{\Lambda} + \gamma$

3. $\rightarrow \Sigma^{o} + \bar{\Lambda}$, $\Sigma^{o} \hookrightarrow \Lambda + \gamma$

4. $\rightarrow \Sigma^{o} + \bar{\Sigma}^{o}$, $\bar{\Sigma}^{o} \hookrightarrow \bar{\Lambda} + \gamma$; $\Sigma^{o} \hookrightarrow \Lambda + \gamma$

5. $\rightarrow \Xi^{o} + \bar{\Xi}^{o}$ [10], $\bar{\Xi}^{o} \hookrightarrow \bar{\Lambda} + \pi^{o}$; $\Xi^{o} \hookrightarrow \Lambda + \pi^{o}$

where the observed Λ appeared in the chamber as a visible $p\pi^{-}$ pair. Reactions 4 and 5 were not treated in the experiment since they appear with two missing neutrals (2 γ's or 2 π^{o}'s) which involve more unknowns than constraining equations.

The weighted average Λ and $\bar{\Lambda}$ effective mass summed over all observed Λ and $\bar{\Lambda}$'s served as a check against systematic errors. This average was defined as:

$$M = \sum_i \left(\frac{M_i}{\delta M_i}\right) \Big/ \sum_i \left(\frac{1}{\delta M_i}\right) \pm 1\Big/\left(\sum_i \left(\frac{1}{\delta M_i}\right)\right)^{1/2}$$

[10] As threshold for this reaction is 2.6 GeV/c, it was possible only at the higher energy.

where M_i = the Λ or $\bar{\Lambda}$ effective mass for event i

δM_i = the error in M_i

The values observed in this experiment were

$M(\Lambda) = 1115.9 \pm .1$
$M(\bar{\Lambda}) = 1115.3 \pm .3$ 2.9 GeV/c $(M(\Lambda) - M(\bar{\Lambda})) = .6 \pm .4$ MeV/c^2

$M(\Lambda) = 1116.1 \pm .1$
$M(\bar{\Lambda}) = 1116.2 \pm .3$ 2.4 GeV/c $(M(\Lambda) - M(\bar{\Lambda})) = .1 \pm .4$ MeV/c^2

which are in reasonable agreement with the accepted mass of the Λ ($1115.6 \pm .08$).

The combined χ^2 distribution for these observed Λ and $\bar{\Lambda}$'s (3-constraint fits) are shown in Figure 6.

Those events where both the Λ and $\bar{\Lambda}$ were observed were usually unambiguously identified as $\Lambda\bar{\Lambda}$, $\Lambda\bar{\Sigma}^o$, $\bar{\Lambda}\Sigma^o$ or $\Lambda\bar{\Lambda}\,\pi^o$ by the kinematics. The final state assignment of the single vee events was not so straightforward. Their final state assignment was determined by looking at the Λ+ missing mass[11] distribution. The peripheral nature of these reactions (as indicated by the angular distributions in Figure 9) produced $\bar{\Lambda}$'s which had very high momentum and as such either had large measurement errors or lived long enough to decay outside the fiducial volume. Thus, the missing mass against the $\bar{\Lambda}$ shown in Figure 7 had both large errors and a depopulation of events in the Λ mass region. Thus, only the missing mass against an observed Λ, weighted by its detection probability, was used to obtain the number

[11] The missing mass is defined as:

$$MM^2 = (E_{\bar{p}} + m_p - E_\Lambda)^2 - (\vec{p}_{\bar{p}} - \vec{p}_\Lambda) \cdot (\vec{p}_{\bar{p}} - \vec{p}_\Lambda).$$

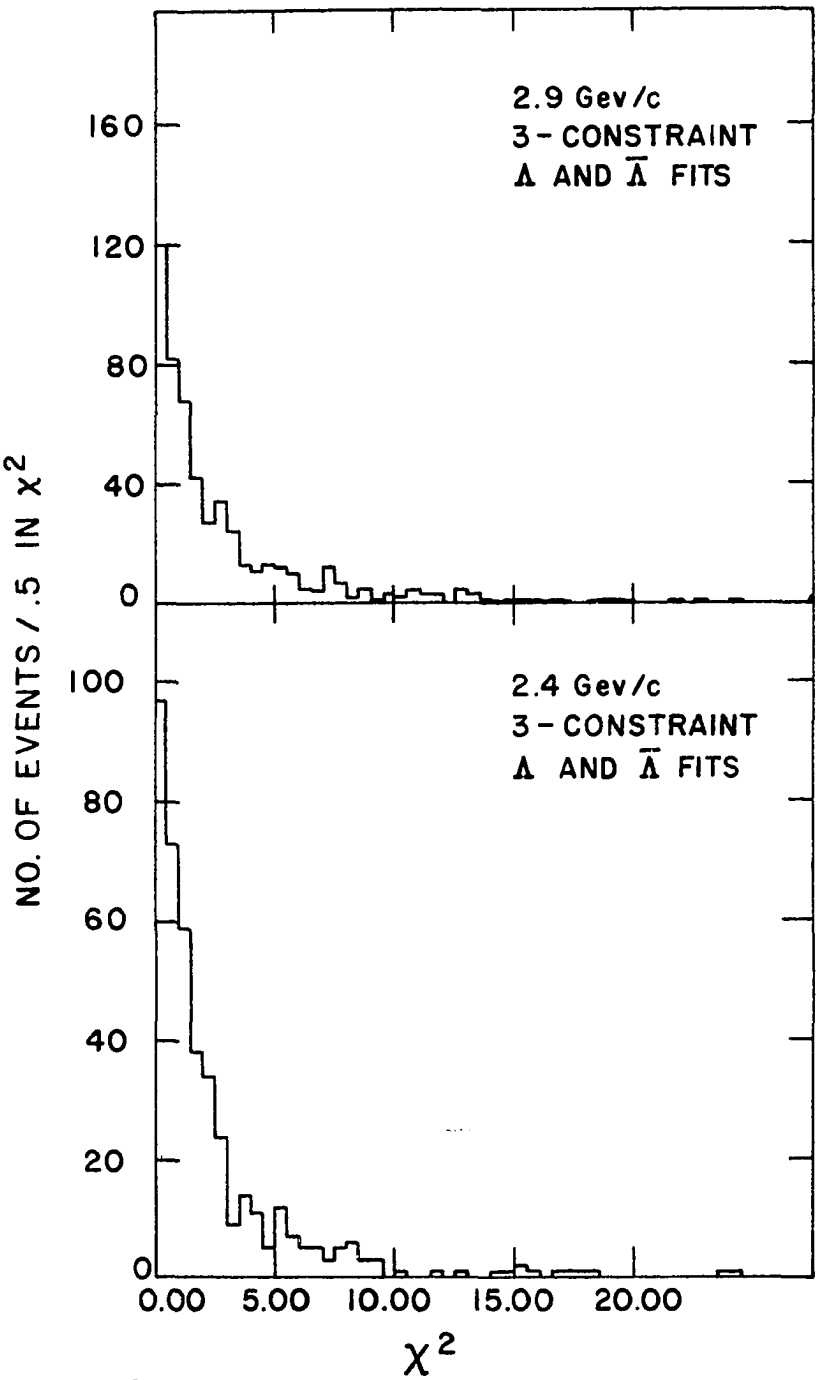

Figure 6. A χ^2 distribution for Λ and $\bar{\Lambda}$ 3-constraint Vee fits

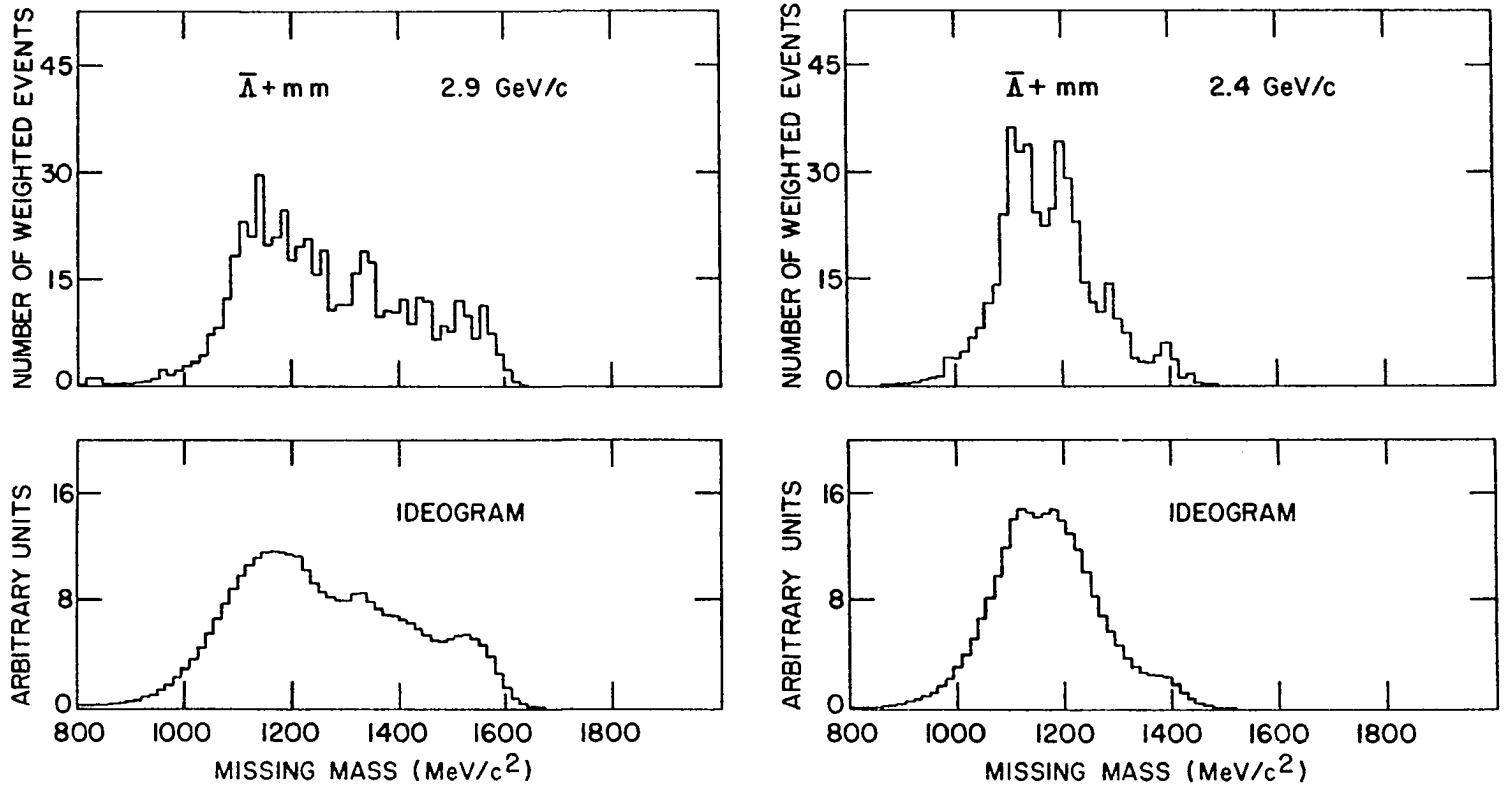

Figure 7. The missing mass against all observed $\bar{\Lambda}$'s. The ideograms indicate large errors

of $\Lambda\bar{\Lambda}$ and $\Lambda\bar{\Sigma}^{o}$ + c.c. events in the experiment.

These Λ plus missing mass distributions (shown in Figure 8 for both energies) had large peaks around the mass of the $\bar{\Lambda}$ and a smaller, well separated, peak at the $\bar{\Sigma}^{o}$ mass. The mass resolution evident from these distributions and further evidenced in the ideograms of Figure 8 justified the final state assignment of these events on the basis of their missing mass alone.

Note that both reaction 2 ($\Lambda\bar{\Sigma}^{o}$) and reaction 3 ($\bar{\Lambda}\Sigma^{o}$) events are included in the Λ+ missing mass plots. They appear in equal numbers since the Λ detection efficiency is the same independent of whether one had observed the direct Λ or a Λ from the $\Sigma^{o} \rightarrow \Lambda\gamma$ decay. These two reactions differ in that the missing mass from reaction 2 should be that of the $\bar{\Sigma}^{o}$, while the missing mass from the reaction 3 will be nearly uniformly spread from 1150 to 1350 at 2.9 GeV/c and from 1145 to 1290 at 2.4 GeV/c.[11]

The Σ^{o} from reaction 4 decays via the electromagnetic interactions to $\Lambda\gamma$ with a lifetime 1×10^{-14} sec. (14), and as such travels $\lesssim 10^{-4}$ cm. from the production vertex before it decays. Thus, the Σ^{o} decay products which appear to come directly from the vertex, also appear in the Λ + missing mass distribution. These events contribute Λ's with a missing mass ranging from 1290 to 1410 at 2.9 GeV/c and from 1210 to 1350 at 2.4 GeV/c.[12]

There are a number of features of these interactions that can be determined by fitting the weighted Λ + MM ideograms:

A. The best missing mass criterion for $\Lambda\bar{\Lambda}$ events.

---

[12] A sample calculation for these missing mass spreads from the $\bar{\Lambda}\,\Sigma^{o}$ and $\Sigma^{o}\Sigma^{o}$ events is made in the Appendix.

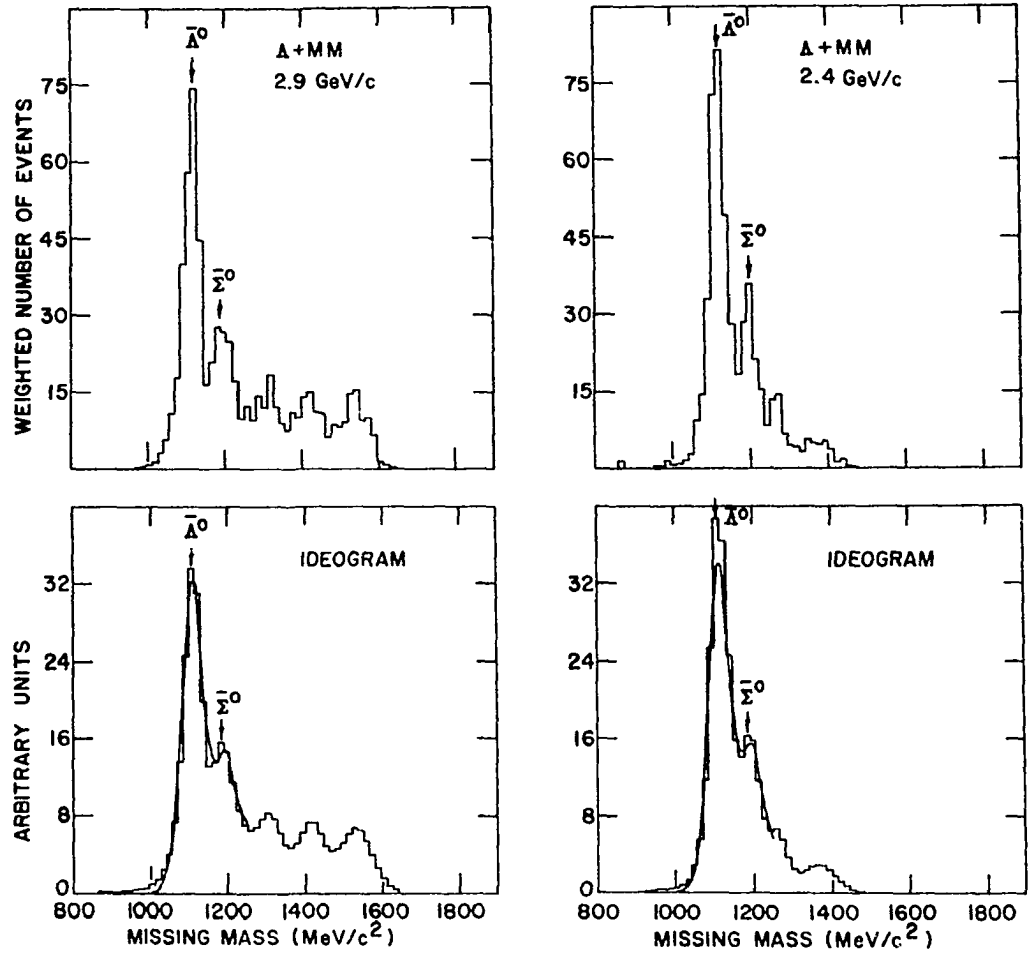

Fig. 8. The missing mass against all observed Λ's. The ideograms show relatively small errors.

B. The percentage contamination in the $\Lambda\bar{\Lambda}$ final state due to $\Lambda\bar{\Sigma}^{o}$ and $\bar{\Lambda}\Sigma^{o}$ events.

C. The validity of identifying all events in the distribution below 1250 MeV as either $\Lambda\bar{\Lambda}$, $\Lambda\bar{\Sigma}^{o}$ or $\bar{\Lambda}\Sigma^{o}$ final states. The limit of 1250 was chosen because it is the lower limit for $\Lambda\bar{\Lambda}\pi^{o}$ events.

The best fits[13] to the data are also shown in Figure 8. The confidence level for these 2 fits are > 95% at 2.4 GeV/c and $\gtrsim$ 85% at 2.9 GeV/c. Accepting all events with a missing mass less than 1160 MeV as $\Lambda\bar{\Lambda}$ events gives a very small contamination between the $\Lambda\bar{\Lambda}$ and $\Lambda\bar{\Sigma}^{o}$ + c.c. final states. The estimated contamination is:

	2.4 GeV/c	2.9 GeV/c
$\Lambda\bar{\Lambda}$ in $\Lambda\bar{\Sigma}^{o}$ + c.c. sample	10%	8.5%
$\Lambda\bar{\Sigma}^{o}$ + c.c. in the $\Lambda\bar{\Lambda}$ sample	5%	5.6%

Thus, the data used in the following discussion of the angular distributions and t distributions for the $\Lambda\bar{\Lambda}$ events contain very little contamination from misidentified events.

The angular distributions of the observed Λ from both the $\Lambda\bar{\Lambda}$ and $\Lambda\bar{\Sigma}^{o}$ + c.c. final states are shown in Figure 9. As was mentioned before, the strong forward peaking of these distributions suggest some type of peripheral exchange mechanism. The diagram for such a process is shown in Figure 10 below:

---

[13] Gaussian distributions with widths and central value free to vary were used for the $\bar{\Lambda}$ and $\bar{\Sigma}^{o}$ peaks and a flat distribution (lower limit of 1150) with amplitude equal to half the $\bar{\Sigma}^{o}$ amplitude was used for the $\bar{\Lambda}\Sigma^{o}$ background.

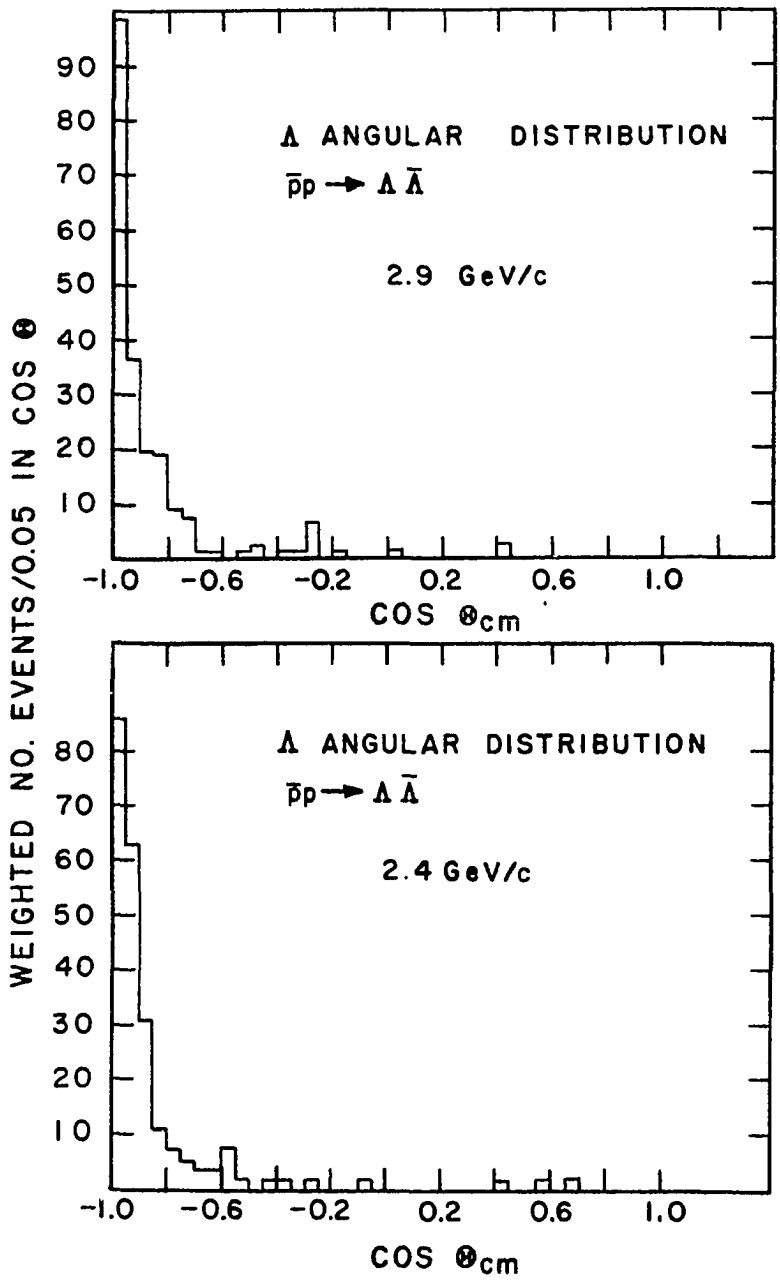

Figure 9. $\Lambda\bar{\Sigma^0}$ + c.c. and $\Lambda\bar{\Lambda}$ angular distribution. θ_{cm} is the angle between the $\Lambda(\Sigma^0)$ and the incident beam in the center of mass

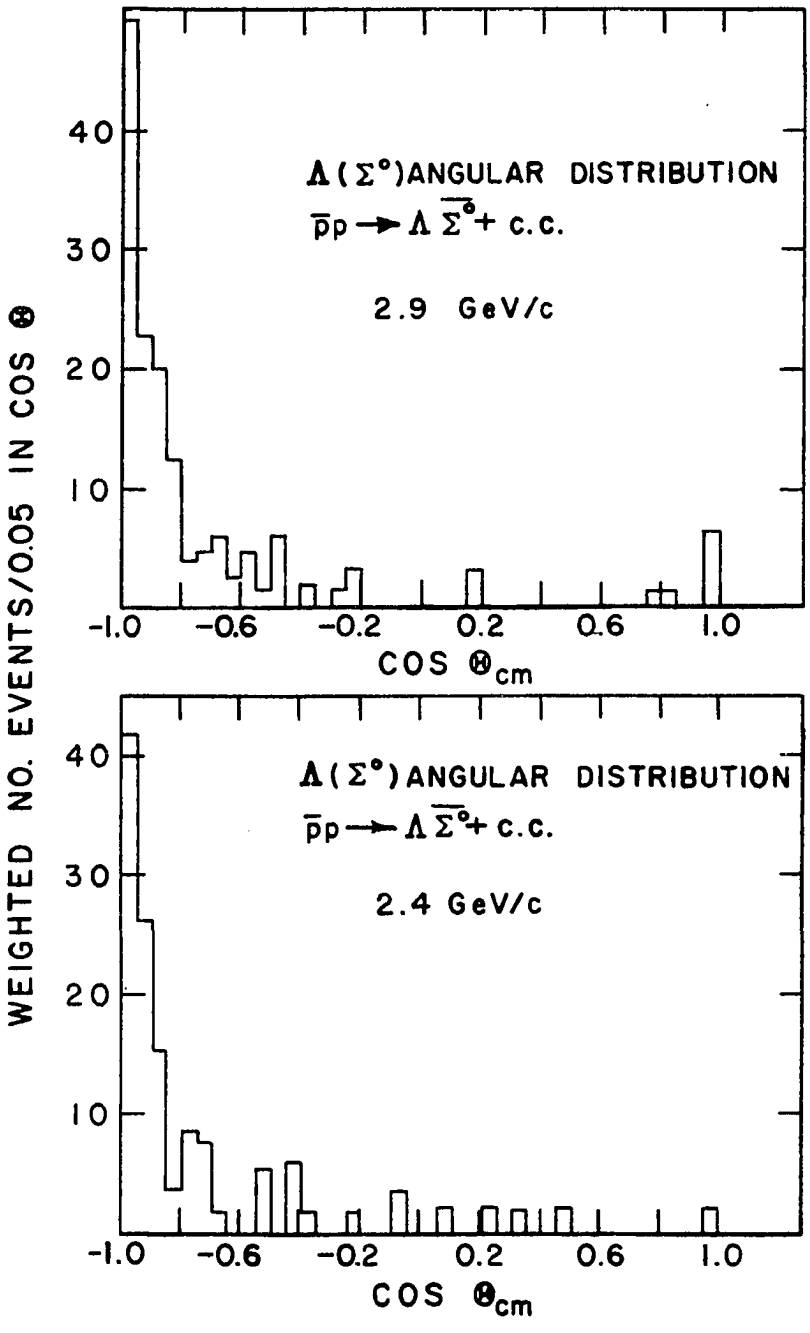

Figure 9. continued

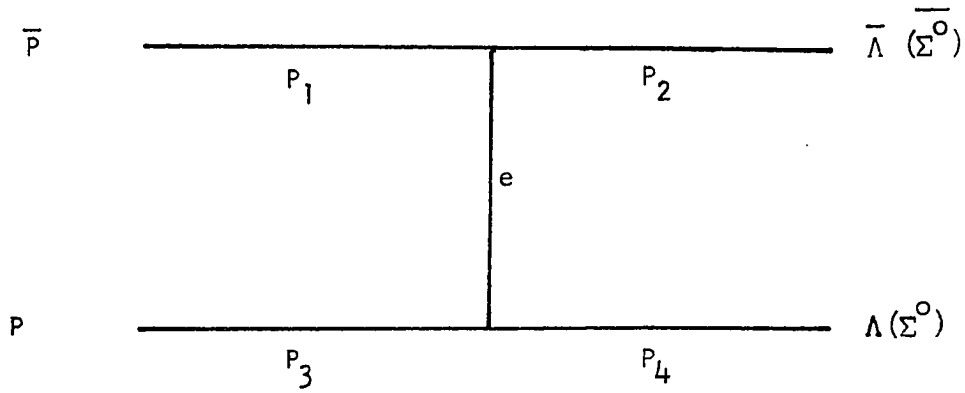

where e is some exchanged particle (or system of particles) with strangeness +1, charge +1, and baryon number 0 (such as a K or $K^*(890)$). P_i is the 4-momentum of a particle in the interaction.

No model known to the author correctly predicts both the observed strong angular dependence of these two final states and the energy dependence of their cross-sections, though attempts have been made to fit the previously available data with any or all of the following models:

1. Single K or K^* exchange (15)
2. Reggeized K^* exchange (16)
3. Mixtures of K and K^* exchange coupled via $\tilde{u}_{12}$ symmetry (17)
4. Mixtures of K and K^* exchange with absorption (18)
5. O(3,1) symmetry (19)

To make a comparison of the experiment with these models, it is convenient to transform the angular distribution into a distribution in t, the square of the four-momentum transfer. t is defined by $-t = (P_2 - P_1)^2$ where P_1 and P_2 are the 4-momenta in Figure 10. P_i has components (p_x, p_y, p_z, i E), the vector momentum and energy of particle i. In terms

of the center of mass scattering angles and the masses:

$$-t = 2\,E_1E_2 - m_1^2 - m_2^2 - 2\,p_1p_2\cos\theta$$

This differential cross-section $\frac{d\sigma}{dt}$ vs. t is shown in Figure 11 for both the $\Lambda\bar{\Lambda}$ and $\Lambda\bar{\Sigma}^0$ + c.c. final states, along with the absorption model prediction of reference 18. This prediction (used for both the 2.4 and 2.9 $\Lambda\bar{\Lambda}$ data) was made for another experiment assuming an incident beam momentum of 3.0 GeV/c. This calculation is not in good agreement with the data from this experiment. As it has been possible to obtain very acceptable fits to the differential cross-section at 3.0, 3.6, 5.7 and 7 GeV/c with this model, it may be possible to redo the calculation using incident momenta of 2.4 and 2.9 GeV/c and obtain agreement with this experiment. Such agreement would be meaningful if the model parameters varied smoothly from those used in the previous experiments.

The polarization of the Λ and $\bar{\Lambda}$ from the reaction has been measured making use of the parity nonconserving decay of the lambdas. The component of the Λ polarization along $\hat{n}$ the normal to the production plane was obtained from:

$$\alpha\,P = 3/N(\sum_i^N \cos\theta_i) \pm \sqrt{3/N}$$

Where N is the number of events, θ_i the pion angle with respect to $\hat{n}$ in the Λ rest frame, and α is the asymmetry parameter in the Λ decay. Using α = .646 $\pm$ .016 (14) gives P_Λ = .26 $\pm$ .11 at 2.4 GeV/c and P_Λ = .24 $\pm$ .12 at 2.9 GeV/c, which is both consistent with zero and consistent with the polarization of .40 $\pm$ .28 seen at 2.5 GeV/c (2). ($P_\Lambda \to 0$ at 3.7 GeV/c (6))

It is possible to extract model independent information about the $\Lambda\bar{\Lambda}$ final state from the angular distribution of the decay products of the Λ and $\bar{\Lambda}$. The probability of the Λ decaying into a solid angle $d\Omega$ is given by:

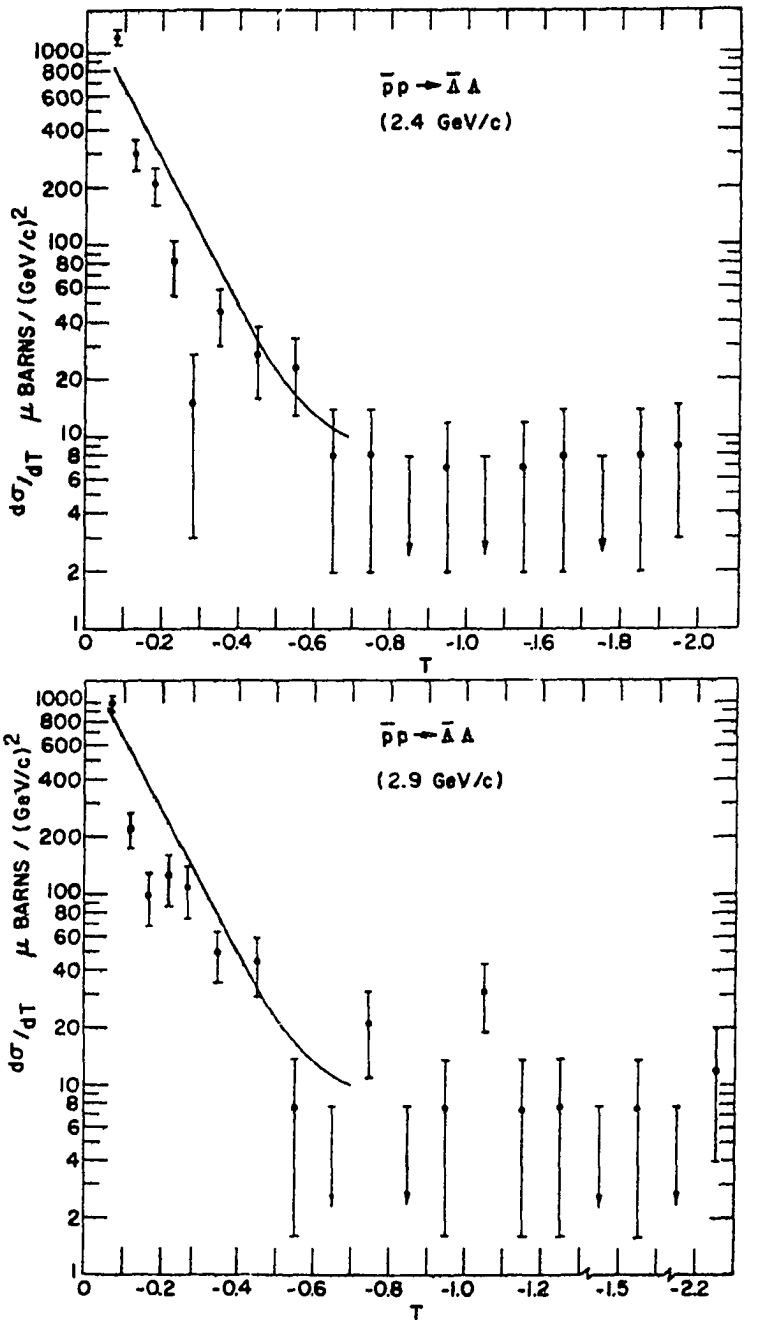

Figure 11. Differential cross sections for $\bar{p}p \to \bar{\Lambda}\Lambda$ and $\bar{p}p \to \Lambda\bar{\Sigma}^0$ + c.c. as a function of t. Arrows indicate no events.

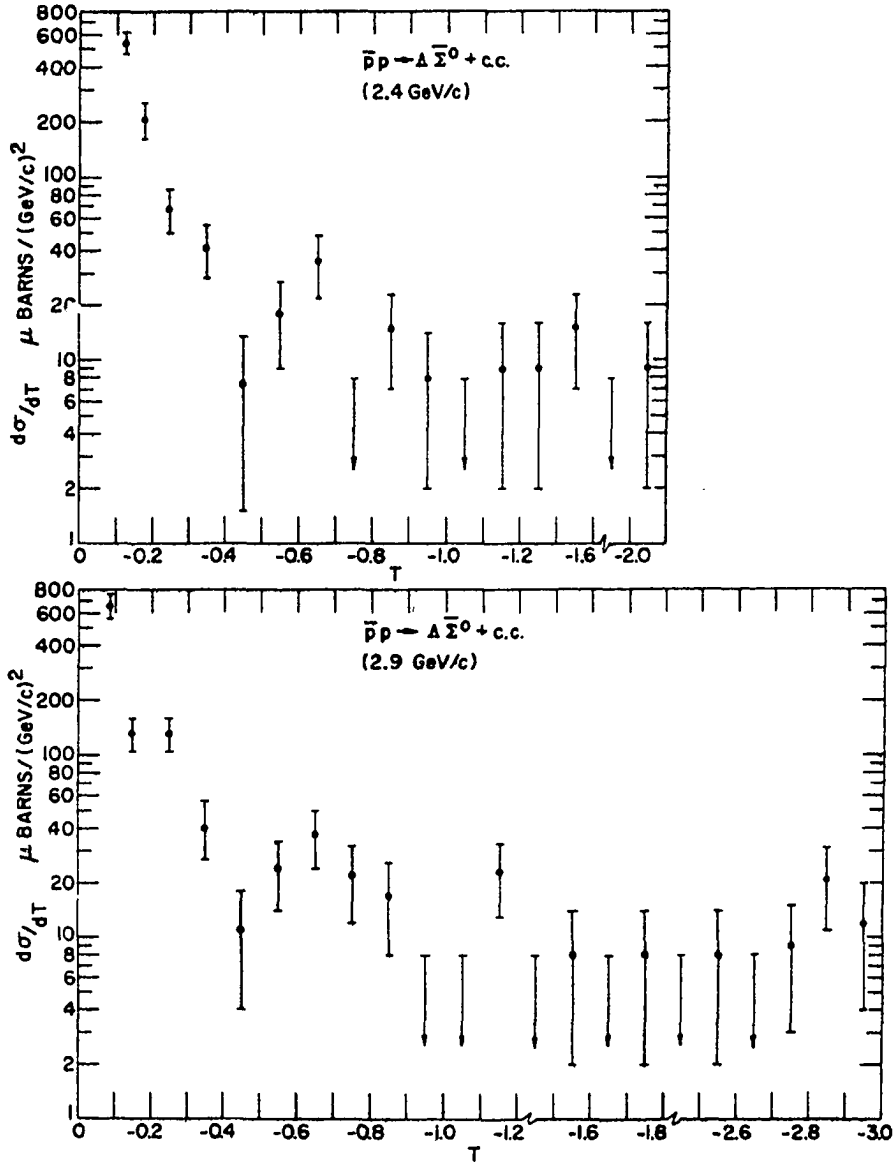

Figure 11. continued

$W(\theta, \varphi) = 1/(2\pi)\{1/2 + (M_+^2 - M_-^2) \sin\theta [\text{Re}\ \rho_{1-1} \cos\varphi - \text{Im}\ \rho_{1-1} \sin\varphi]\}$[14]

where θ and φ are defined in the Λ rest frame with the z axis taken as the incident beam direction and the y axis taken to be normal to the production plane. The ρ's are production density matrix elements with $\rho_{2n,2n'}$ being the product of Λ amplitudes with spin projections n and n'. Thus, ρ_{11} = probability for forming the Λ with spin projection +1/2. $M_+^2(M_-^2)$ is the probability of the P from the Λ decay having its spin aligned (anti-aligned) with its direction of motion. It is of particular interest to present these density matrix elements for the $\Lambda\bar{\Lambda}$ final state since it is one of the few final states where the imaginary part of the density matrix can be determined.[15] A peripheral model (i.e., one which uses diagrams like Figure 10) predicts these imaginary parts to be zero independent of the spin, coupling constants, mass, etc., of the exchanged system. (20) Thus, their determination is a direct test of this model.

Integrating out the φ dependence gives a prediction for a constant θ dependence which is consistent with the data shown in Figure 12.

To pick out a specific density matrix element (to within a multiplying constant of $(M_+^2 - M_-^2)$), one can take an average value over specific trigonometric functions. These average values are defined by:

$$\langle f(\theta, \varphi)\rangle = \int_0^{2\pi} \int_{-1}^{1} f(\theta, \varphi) W(\theta, \varphi)\, d(\cos\theta)\, d\varphi$$

and determined from the data via $\langle f(\theta, \varphi)\rangle = 1/N \sum_{i=1}^{N} f(\theta, \varphi)$ where N = number of events.

Expressions for the individual ρ's are given below together with their values as determined from this experiment:

---

[14] This form has been derived using reference 21 as a starting place.

[15] This is a result of the parity violating decay of the $\bar{\Lambda}$.

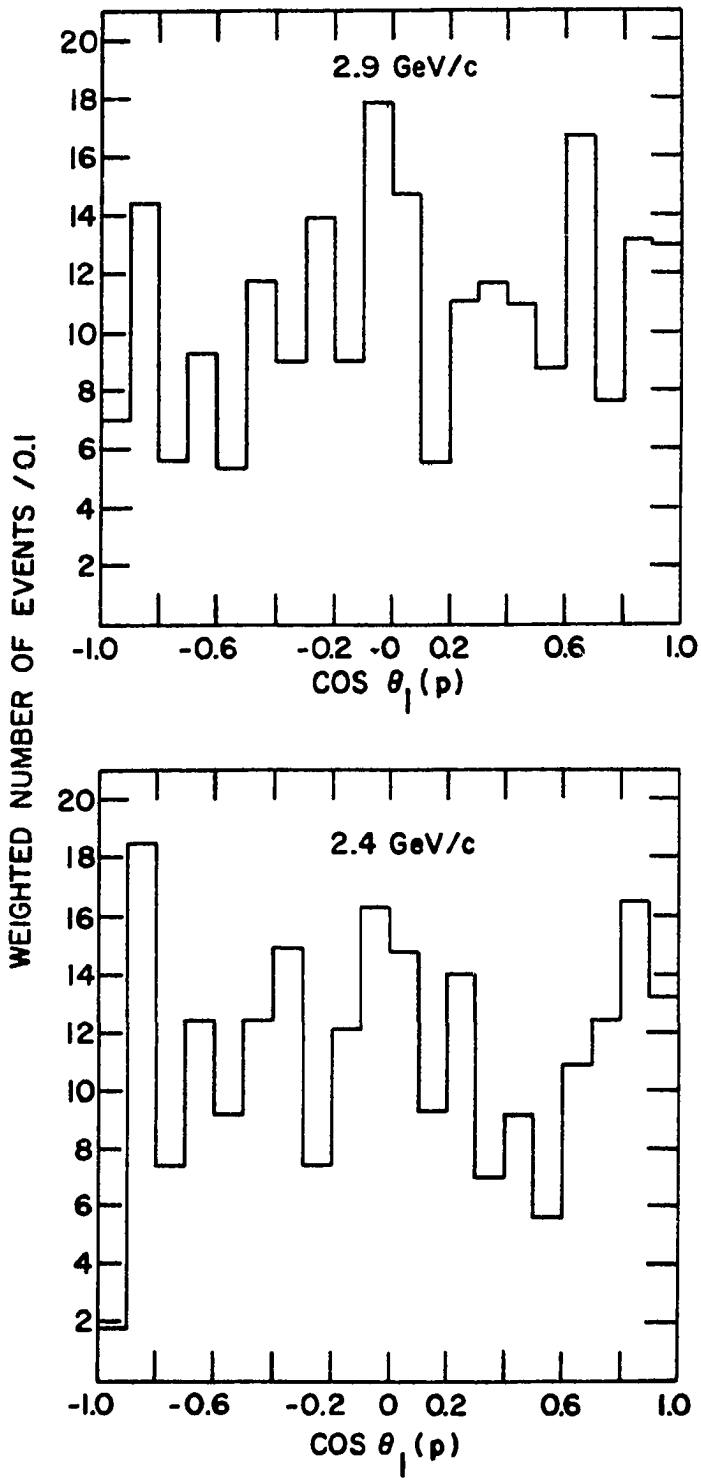

Figure 12. Proton angular distribution in the Λ rest frame wrt the Λ direction

	2.4 GeV/c	2.9 GeV/c
$(M_+^2 - M_-^2)$ Re $\rho_{1-1} = 4/\pi \langle \cos \varphi \rangle =$	$.03 \pm .11$	$.02 \pm .10$
$(M_+^2 - M_-^2)$ Im $\rho_{1-1} = -4/\pi \langle \sin \varphi \rangle =$	$.02 \pm .11$	$.03 \pm .09$

The maximum amount of information on the production mechanism is given by the analysis of the joint decay distributions, (20) where seven more production amplitudes can be determined.

The joint decay distribution is given by;

$$W(\theta_1 \varphi_1, \theta_2 \varphi_2) = \frac{1}{4\pi^2} \{\frac{1}{4} + \frac{1}{4}(M_+^2-M_-^2)^2 (4\rho_{11}^4 - 1) \cos\theta_1 \cos\theta_2$$

$$+\frac{1}{2} (M_+^2-M_-^2)^2 \rho_{1-1}^{1-1} \sin\theta_1 \sin\theta_2 \cos(\varphi_1+\varphi_2)$$

$$+\frac{1}{2} (M_+^2-M_-^2)^2 \rho_{1-1}^{-11} \sin\theta_1 \sin\theta_2 \cos(\varphi_1 - \varphi_2)$$

$$+ (M_+^2-M_-^2)^2 \text{ Re } \rho_{1-1}^{11} \sin\theta_1 \cos\theta_2 \cos\varphi_1$$

$$- (M_+^2-M_-^2) \text{ Im } \rho_{1-1}^{11} \sin\theta_1 \sin\varphi_1$$

$$+ (M_+^2- M_-^2)^2 \text{ Re } \rho_{11}^{1-1} \sin\varphi_2 \cos\theta_1 \cos\varphi_2$$

$$- (M_+^2 - M_-^2) \text{ Im } \rho_{11}^{1-1} \sin\varphi_2 \sin\varphi_2 \}$$

with the individual density matrix elements (denoted by $\rho^{2n_1, 2n'_1}_{2n_2, 2n'_2}$) and their experimental values given by:

	2.4 GeV/c	2.9 GeV/c
$(M_+^2-M_-^2)^2(4\rho_{11}^{11} - 1) = 9\langle \cos\theta_1 \cos\theta_2 \rangle =$	$.28 \pm .23$	$-.18 \pm .27$

	2.4 GeV/c	2.9 GeV/c
$(M_+^2-M_-^2)^2\,\rho_{1-1}^{1-1} = \frac{16}{\pi^2}[\langle\cos\varphi_1\cos\varphi_2\rangle -$		
$\langle\sin\varphi_1\sin\varphi_2\rangle] =$	$.00 \pm .10$	$.00 \pm .09$
$(M_+^2-M_-^2)^2\,\rho_{1-1}^{-11} = \frac{16}{\pi^2}[\langle\cos\varphi_1\cos\varphi_2\rangle +$		
$\langle\sin\varphi_1\sin\varphi_2\rangle] =$	$.01 \pm .10$	$-.03 \pm .09$
$(M_+^2-M_-^2)^2\,\mathrm{Re}\,\rho_{1-1}^{11} = \frac{16}{\pi^2}\langle\sin 2\theta_2\cos\varphi_1\rangle =$	$.03 \pm .08$	$-.00 \pm .07$
$(M_+^2-M_-^+)\,\mathrm{Im}\,\rho_{1-1}^{11} = -2/\pi\,\langle\sin\varphi_1\rangle =$	$.04 \pm .03$	$.01 \pm .04$
$(M_+^2-M_-^2)^2\,\mathrm{Re}\,\rho_{11}^{1-1} = \frac{16}{\pi^2}\langle\sin 2\,\theta,\cos\varphi_2\rangle =$	$.01 \pm .06$	$-.02 \pm .07$
$(M_+^2-M_-^2)\,\mathrm{Im}\,\rho_{11}^{1-1} = -2/\pi\,\langle\sin\varphi_2\rangle =$	$-.03 \pm .04$	$-.01 \pm .03$

Again it is possible to determine these density matrix elements only to within a constant. As for the single decay density matrix, the exchange model predicts all imaginary parts = 0. This prediction is seen to be in good agreement at 2.9 and in reasonable agreement at 2.4 GeV/c.

The exchange model also predicts no t dependence. To the extent that 160 events allow a determination of the t dependence, these distributions (displayed in Figures 13 and 14) were examined at both momenta.

The data do not show a strong dependence on t in the 2.9 data. However, the 2.4 data does seem to indicate some variation of the density matrix with t. (It should be pointed out that within the statistics these data are also consistent with no t dependence.)

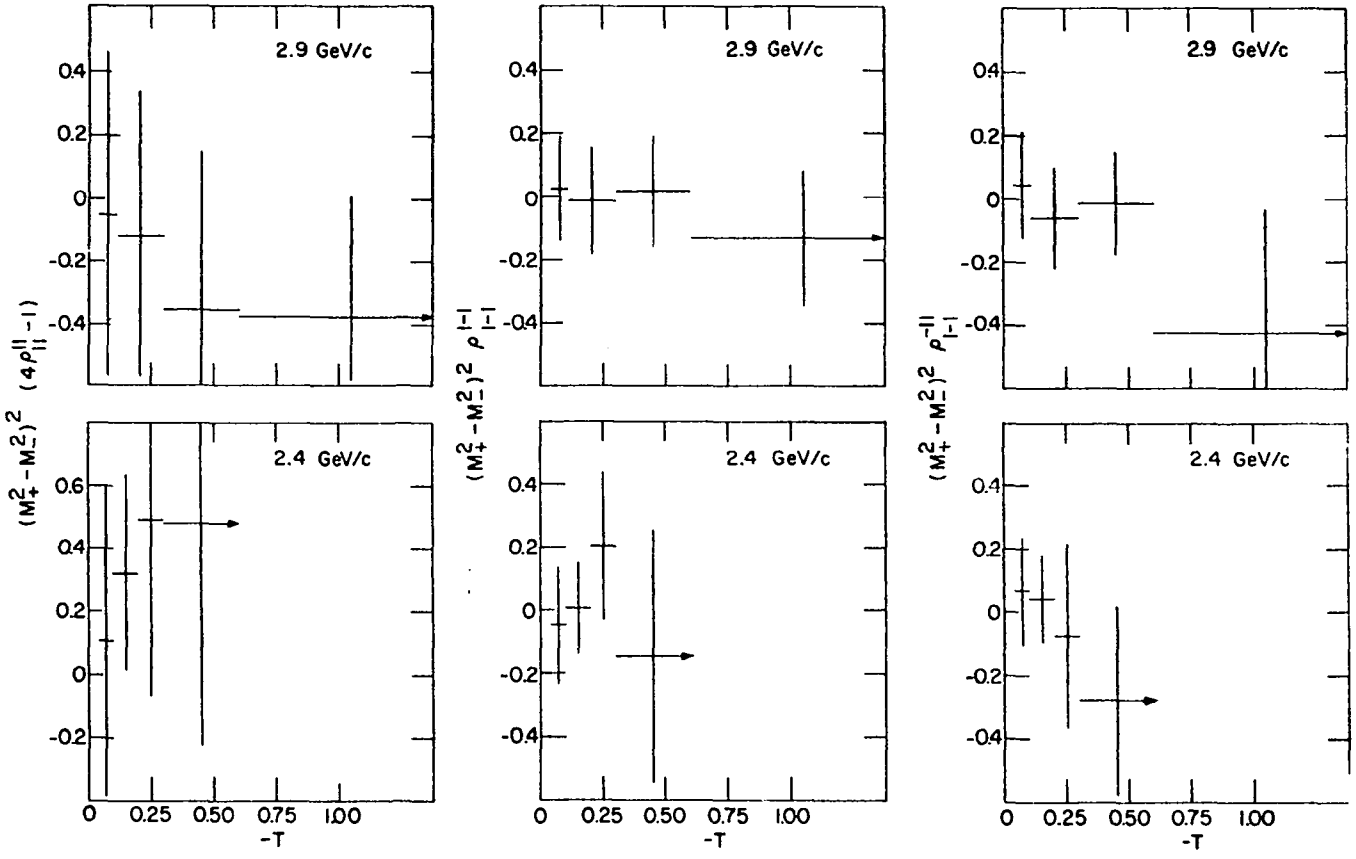

Fig. 13. Joint spin-density matrix elements for $\Lambda\bar{\Lambda}$ production

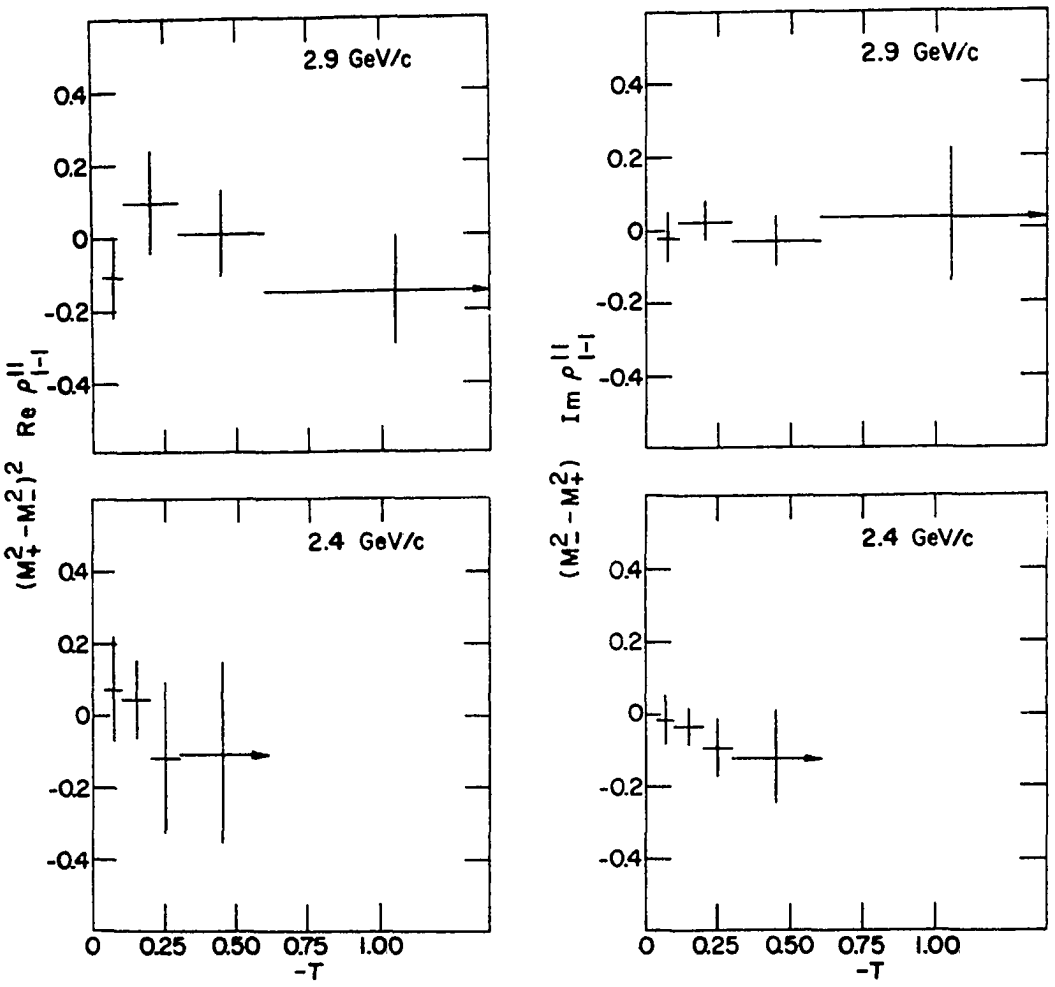

Fig. 14a. Joint spin-density matrix elements for $\Lambda\bar{\Lambda}$ production

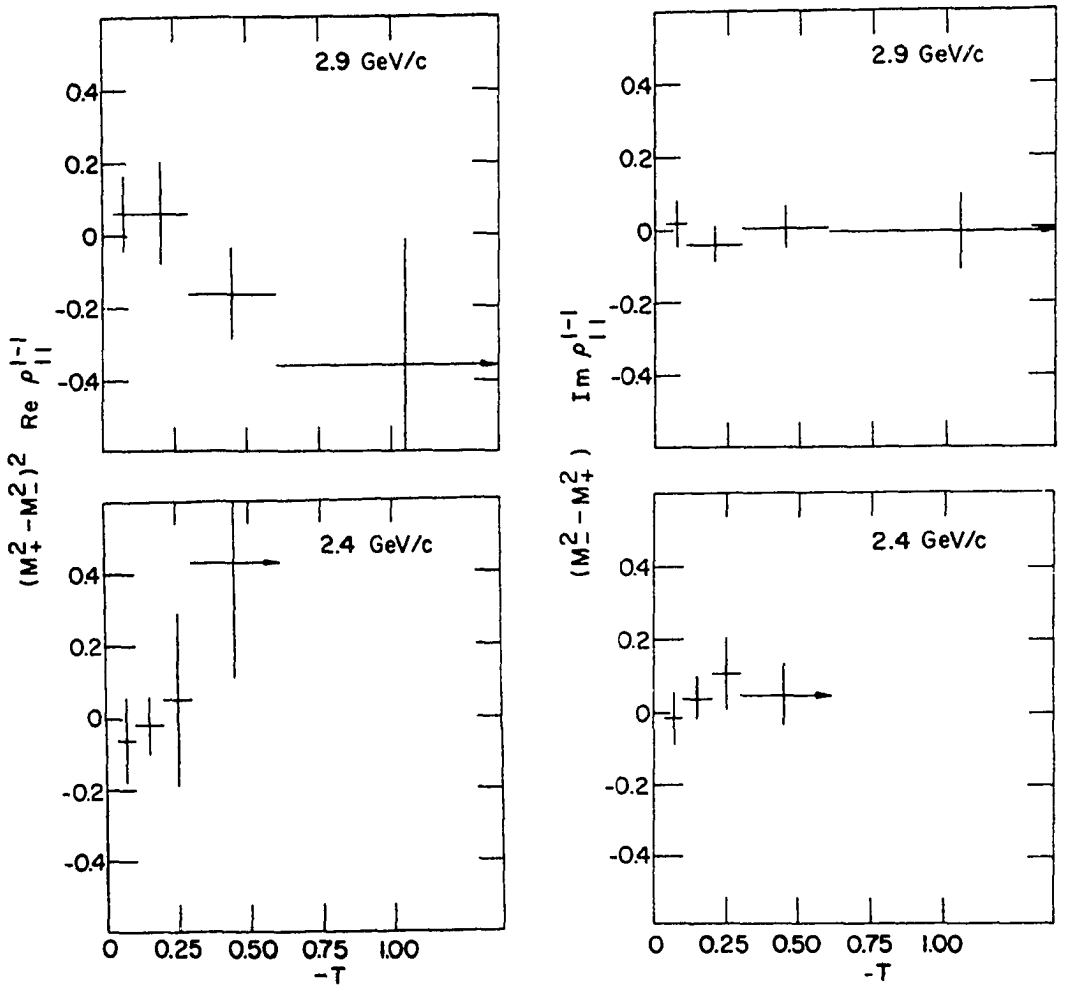

Fig. 14b. Joint spin-density matrix elements for $\Lambda\bar{\Lambda}$ production

B. Charged 2-Body Final States

The observed reactions were:

1. $\bar{p} + p \rightarrow \Sigma^+ + \overline{\Sigma^+}$
2. $\bar{p} + p \rightarrow \Sigma^- + \overline{\Sigma^-}$
3. $\bar{p} + p \rightarrow \Xi^- \overline{\Xi^-}$

Their possible decay products and accepted decay ratios are given below:

$\Sigma^+ \rightarrow p\pi^-$	$52.8\% \pm 1.5\%$
$\rightarrow \pi^o N$	$47.2\% \pm 1.5\%$
$\Sigma^- \rightarrow n\pi^-$	100%
$\Xi^- \rightarrow \Lambda\, \pi^-$	100%

Reaction 3 was uniquely identified as the Λ and/or $\bar{\Lambda}$ decay was also seen. The three events found in this experiment were added to those found at 3.0 and 3.7 GeV/c and the angular distribution for the published world's supply of $\overline{\Xi^-}$'s from 2-body $\Xi^-\overline{\Xi^-}$ events is shown in Figure 15. There is a tendency for the $\overline{\Xi^-}$ to be correlated with the incident $\bar{P}$ but this correlation is definitely not very strong. This plus the small cross-section is indicative of the fact that there is no known particle with Q = 2 and S = 2 which could be exchanged to produce this final state. Reactions 2 and 3 involved a number of experimental difficulties, some of which have already been mentioned. The charged Σ decays to one charged and one neutral (unseen) particle, and their track lengths are often so short that only their production angles can be measured. Thus, these Σ decay fits involve four unknowns: the three components of the momentum of the

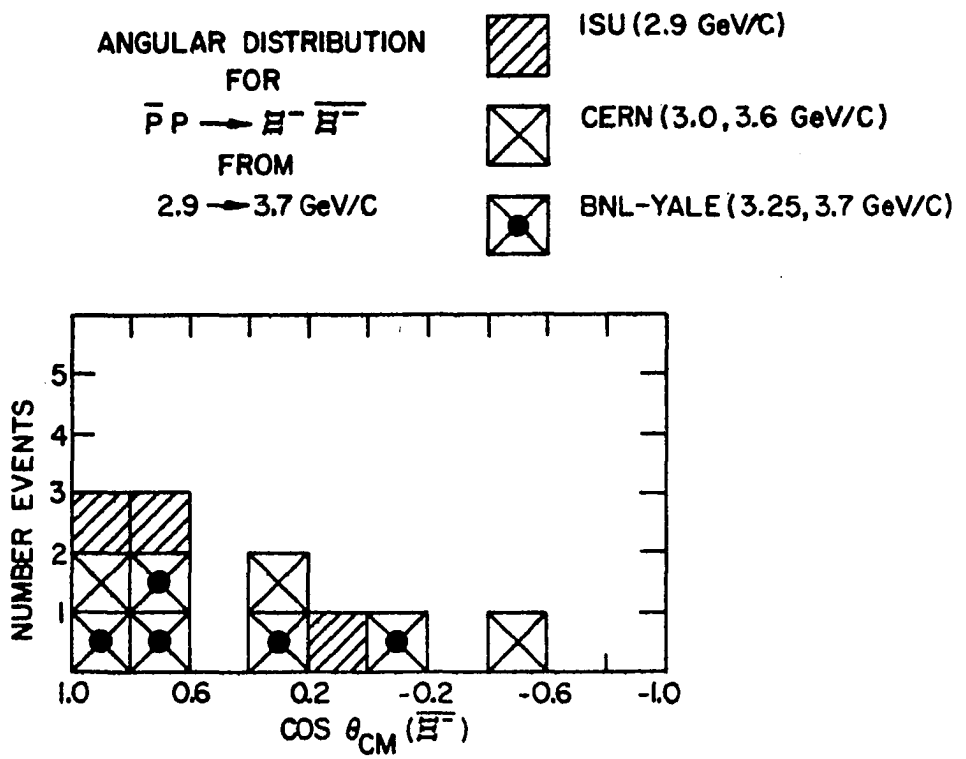

Figure 15. Center of mass angular distribution for $\bar{\Xi}^-$ from $\bar{p}p \rightarrow \Xi^- \bar{\Xi}^-$ events

neutral particle and the magnitude of the momentum of the Σ. With four unknown quantities and only four equations (three from momentum conservation and one from energy conservation), the fitting equations degenerate to a simple solution for these unknown variables. This does not allow for any measurement error in events especially difficult to measure. It was thus decided that the 2-prong 1-decay events would be so ambiguous as to be meaningless. Therefore, the $\Sigma\bar{\Sigma}$ final states were investigated using only those events in the 2-prong 2-decay topology. Due to the $\Sigma^+ - \Sigma^-$ mass difference of only 8 MeV, mentioned earlier, these double decay events were uniquely identified only if the $\Sigma^+ (\bar{\Sigma}^+)$ was observed to decay via the $P(\bar{P})$ decay mode. Listed below is the number of unique $\Sigma^+\bar{\Sigma}^+$ and ambiguous ($\Sigma^+\bar{\Sigma}^+ + \Sigma^-\bar{\Sigma}^-$) events for both momenta.

	2.4 GeV/c	2.9 GeV/c
Unique	21	19
Ambiguous	35	32

The weighted angular dependence of these events is shown in Figure 16. As with the neutral final states the Σ's are observed to be peripherally produced. This peripheral production is painfully evident in the subsequently biased sample of $\bar{\Sigma}^+$'s obtained. For a $\bar{\Sigma}^+$ produced at 30° in the center of mass the resulting proton decay angle between the direction of the Σ and the direction of the subsequent proton from the decay in the laboratory is $\lesssim 8^\circ$ and the decay angle observed on the film is the projection of this angle in 3-dimensional space. Thus, these events were often difficult to spot and were preferentially missed in the scan. To correct this bias, all decays with a decay angle less than 4° were deleted from the data and lost events corrected for in the following manner. The Σ^+ was assumed to

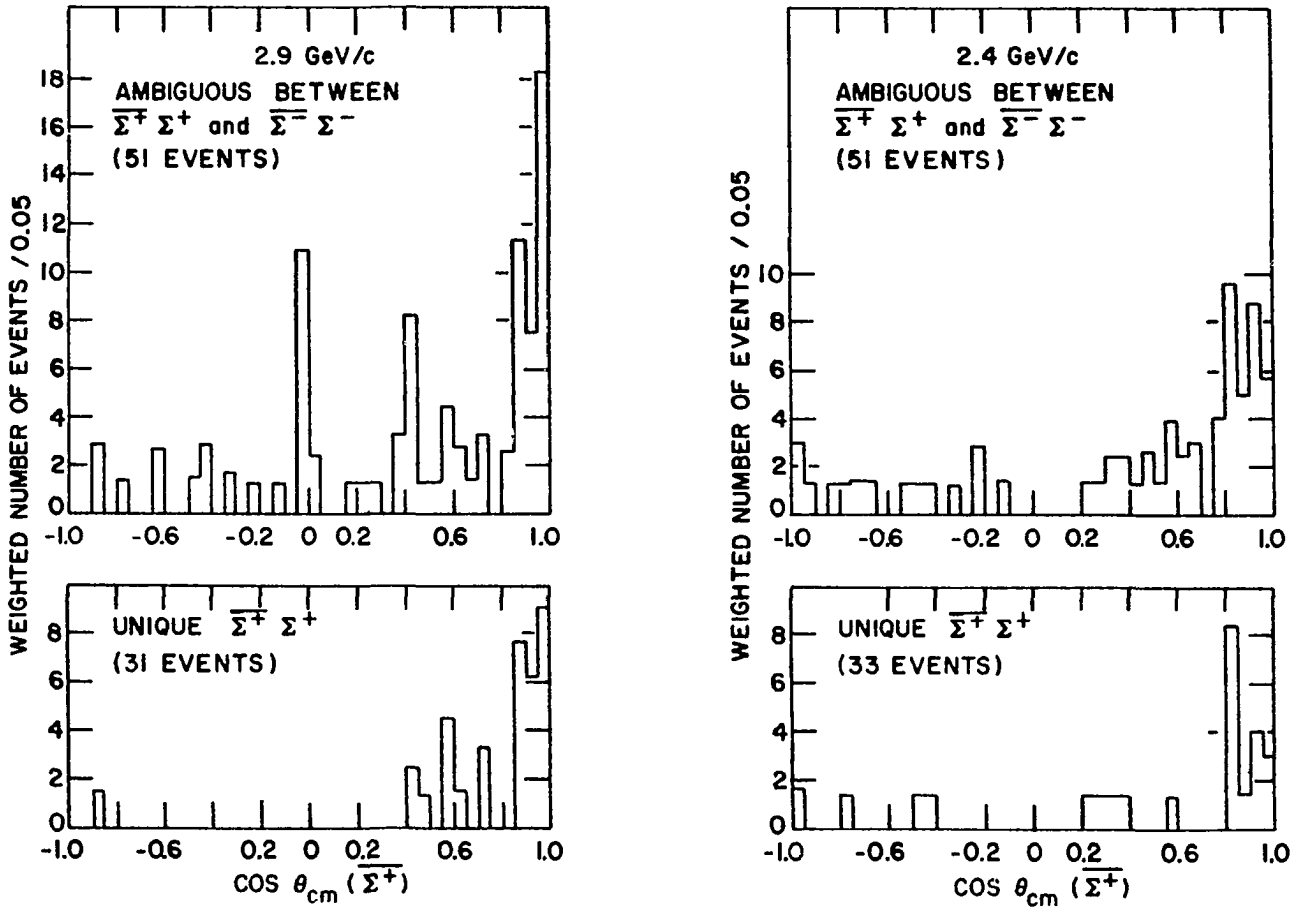

Figure 16. Center of mass angular distribution for $\overline{\Sigma^+}(\Sigma^-)$ from unique and ambiguous events. (The bin $-.05 \leq \cos \text{ and } \leq 0$ contains one event. It is probably more reasonable to use the average weight of 2.)

be associated with the target proton and therefore, to have low laboratory momentum. Thus, the $\Sigma^+\overline{\Sigma^+}$ cross-section was obtained by assuming the total number of events to be twice the weighted number of events where the Σ^+ was observed to decay to $p\pi^o$. The number of Σ's in each category, is listed below:

	2.4 GeV/c	2.9 GeV/c
$\Sigma^+ \to p\pi^o\ \overline{\Sigma^+} \to \bar{p}\ \pi^o$	4	2
$\Sigma^+ \to p\pi^o\ \overline{\Sigma^+} \to \pi^+ N$	13	11
$\Sigma^+ \to \pi^+ N\ \overline{\Sigma^+} \to \bar{p}\ \pi^o$	4	6
$\Sigma^+ \to \pi^+ N\ \overline{\Sigma^+} \to \pi^- \bar{N}$ $\Sigma^- \to \pi^- N\ \overline{\Sigma^-} \to \pi^+ \bar{N}$	35	32

It was decided that any attempt to subtract out the $\Sigma^-\overline{\Sigma^-}$ events from the $\Sigma^+\overline{\Sigma^+}$ events with these statistics and the known bias would not be meaningful, so all cross-sections are quoted as combined $\Sigma^+\overline{\Sigma^+} + \Sigma^-\overline{\Sigma^-}$.

C. Comparison with SU_3

The protons, antiprotons, kaons, and all observed particles in the 2-body final states are members of SU_3 octets. Thus, the suggested K or K^* exchange dominance is represented by an octet exchange between two $8 \otimes 8$ representations. The two types of independent octet couplings, symmetric (D-type), and anti-symmetric (F-type) have been calculated by Tanaka (22). The data previously available from 2.7→6.9 GeV/c has been compared with the branching ratios predicted by these couplings with the following results: Good agreement with the anti-symmetric coupling and disagreement with the symmetric coupling. (8). The results of this experiments are given in Table V. It also shows agreement with F-type coupling and disagreement with D-type.

Table V. Cross-sections compared to predictions of the two different octet couplings

Final State →	$\Lambda\bar{\Lambda}$	$\Lambda\bar{\Sigma}^0$ + c.c.	$\Sigma^+\bar{\Sigma}^+$	$\Sigma^0\bar{\Sigma}^0$
$\frac{2.4}{\sigma}$	$120 \pm 11\mu b$	$61 \pm 7\mu b$	$47 \pm 8\ \mu b$	$< 27\ \mu b$
ratio[a]	$9 \pm .8$	$5 \pm .6$	$4.3 \pm .7$	< 2.4
$\frac{2.9}{\sigma}$	$113 \pm 10\mu b$	$71 \pm 8\mu b$	$43 \pm 8\mu b$	$< 26\ \mu b$
ratio[a]	$9 \pm .8$	$6.2 \pm .7$	$4.1 \pm .7$	< 2.5
symmetric (D) coupling	1 :	6 :	36 :	9
anti-symmetric (F) coupling	9 :	6 :	4 :	1

[a]The $\Lambda\bar{\Lambda}$ cross section was normalized to 9 to calculate these ratios.

V. 3 AND 4 BODY FINAL STATES

Those 3 and 4 body hyperon-antihyperon final states studied are listed along with the number of observed unweighted events in Table VI.

As it was energetically possible to produce the three known resonant states below:

Symbol (Mass)	Width (MeV)	Relevant Decay Modes
Σ (1385)	35 ± 3	$\Lambda\pi$ 90% $\Sigma\pi$ 10%
Λ (1404)	40 ± 10	$\Sigma\pi$ 100%
Σ (1550)	16 ± 2	$\Sigma\pi$ 45%

it is of interest to look for their production in the $\Sigma\pi$ and $\Lambda\pi$ effective mass distributions. Shown in Figure 17 is a scattergram of the $\Lambda\pi$ effective mass vs. the $\Sigma\pi$ effective mass from the $\bar{\Lambda}\Sigma^- \pi^+$ + c.c. and $\bar{\Lambda}\Sigma^+ \pi^-$ + c.c. final states. A similar plot of the $\bar{\Lambda}\pi^o$ vs. $\Lambda\pi^o$ masses from the $\Lambda\bar{\Lambda}\pi^o$ final states along with a nonresonant phase space distribution on each of the projected histograms is shown in Figure 18. In the $\bar{\Lambda}\Sigma\pi$ + c.c. plot, there are departures from phase space at 1400 MeV in the $\Lambda\pi$ projection, and at 1375 and 1525 in the $\Sigma\pi$ projection. The enhancement centered at 1375 in the $\Sigma\pi$ mass distribution is interpreted to be the $\Lambda(1404)$ [rather than $\Sigma(1385)$] production for the following reason. $\Sigma(1385)$ has a 10% decay to $\Sigma\pi$ and a 90% decay to $\Lambda\pi$. The observed 1385 enhancements in the $\Lambda\pi$ channels are <u>at best</u> four times that seen in the $\Sigma\pi$ channel. The reason for the mass shift is unknown. A more detailed look at the $\Sigma\pi$ + c.c. effective mass distribution shows that, although both $\Sigma^+\pi^-$ + c.c. and $\bar{\Sigma}^+\pi^+$ + c.c. contribute equally (within statistics) to the two observed enhancements, the $\Lambda\pi^+$ + c.c. events contribute much more than do the $\Lambda\pi^-$ + c.c. events. This feature of the data has been

Table VI. Numbers of events observed in the 3 and 4 body hyperon-antihyperon final states studied

	Number of Events	
	2.4	2.9
1. $\Sigma^+ \pi^- \bar{\Lambda}$ + c.c.	3	31
2. $\Sigma^- \pi^+ \bar{\Lambda}$ + c.c.	5	21
3. $\Sigma^+ \overline{\Sigma^0} \pi^-$ + c.c.	0	3
4. $\Sigma^- \overline{\Sigma^0} \pi^+$ + c.c.	0	4
5. $\Lambda \bar{\Lambda} \pi^0$	9	46
6. $\Sigma^{\pm} \overline{\Sigma^{\pm}} \pi^0$ + c.c.	0	3
7. $\Sigma^{\pm} \bar{\Lambda} \pi^{\mp} \pi^0$ + c.c.	0	3
8. $\Lambda \bar{\Lambda} \pi^+ \pi^-$	0	5

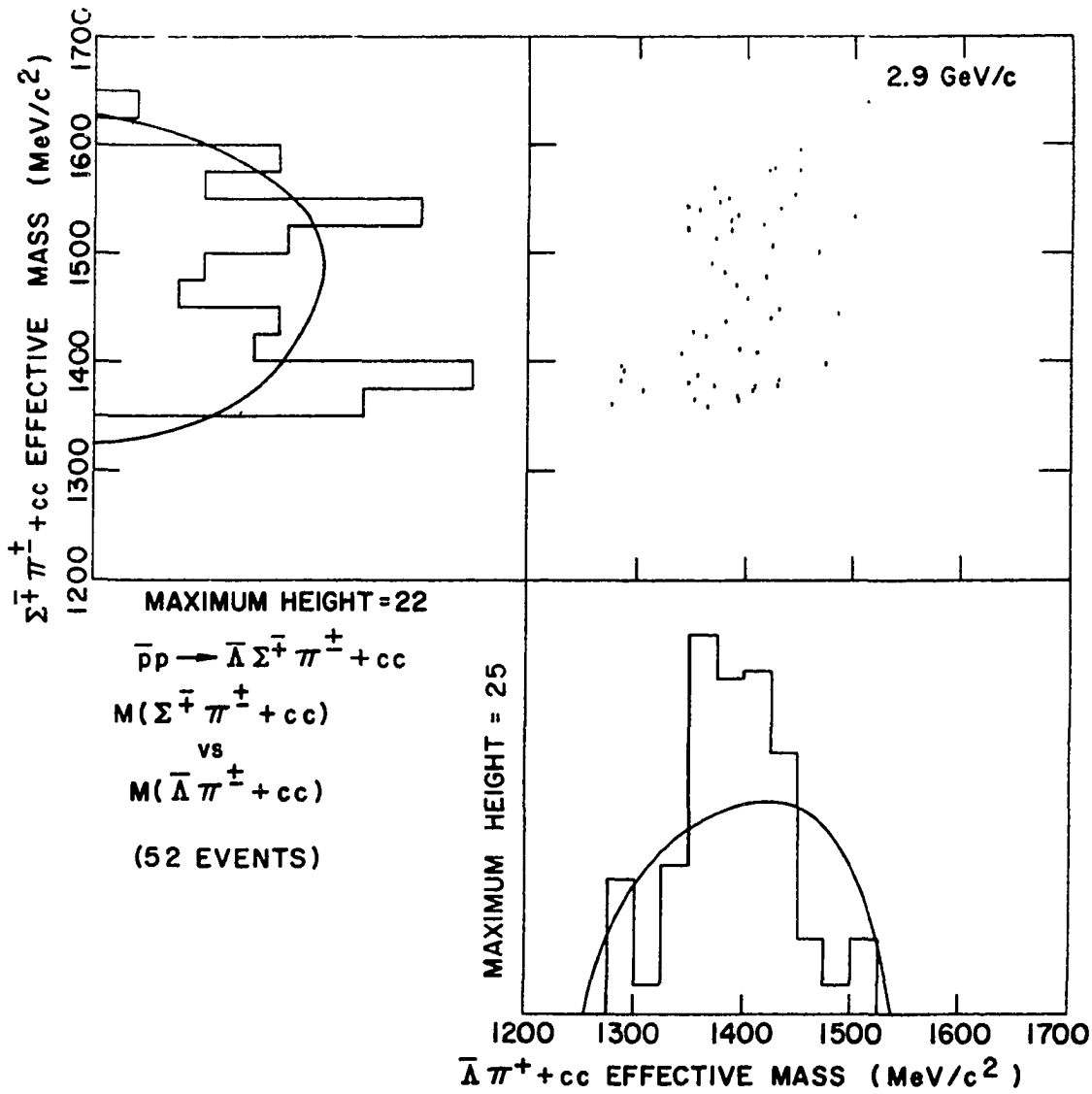

Figure 17. Scattergram of $\bar{\Lambda}\,\pi^{\pm}$ + c.c. effective mass versus the $\Sigma^{\mp}\,\pi^{\pm}$ + c.c. effective mass for $\bar{p}p \rightarrow \bar{\Lambda}\,\Sigma^{\mp}\,\pi^{\pm}$.

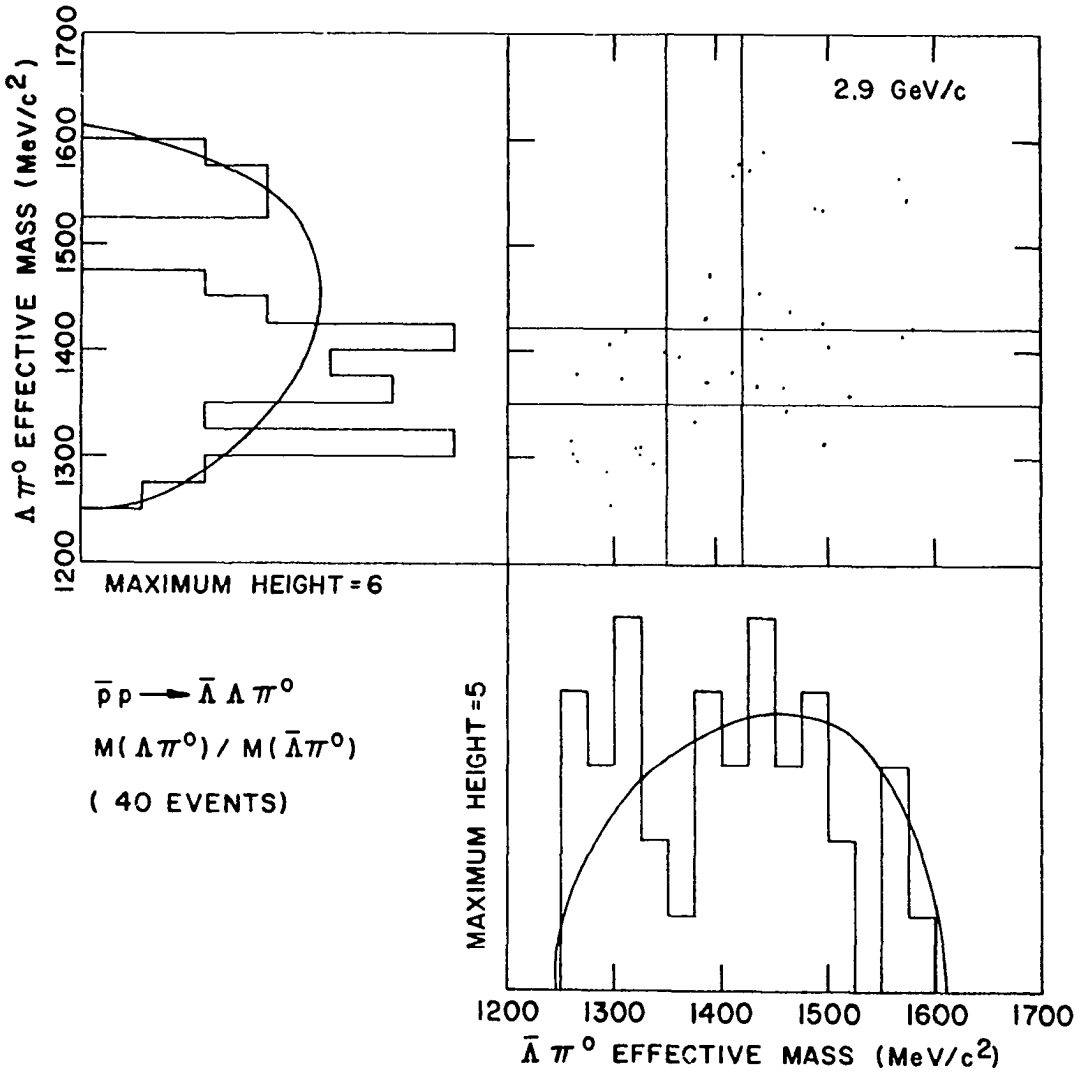

Fig. 18. Scattergram of $\Lambda\ \pi^0$ effective mass versus $\bar{\Lambda}\ \pi^0$ effective mass for $\bar{p}p \rightarrow \Lambda\bar{\Lambda}\ \pi^0$ events. The horizontal and vertical bands enclose the accepted values for the $\Sigma(1385)$

seen before at somewhat higher energies (4).

A look at the possible exchange diagrams which could be responsible for a $\Lambda\pi$ resonance shows that to produce a $\Lambda\pi^-$ or $\bar{\Lambda}\pi^+$ system requires the exchange of a particle with either double charge or baryon number +2. The fact that no such particles have been observed may be one reason for the small amount of $\Lambda\pi^-$ + c.c. resonance produced. (A $\Lambda\pi^+$ + c.c. resonance can be produced assuming the exchange of a K or $K^*(890)$). The relevant diagrams for the $\Sigma^+\bar{\Lambda}\pi^-$ + c.c. and $\Sigma^-\bar{\Lambda}\,\pi^+$ + c.c. final states are shown in Figure 19.

A rather interesting feature of these two final states is their production angular distribution. Only those reactions in which Σ (1385) production was allowed by a one-particle exchange model were peripherally produced. Even this peripheral production was weak. The other reactions allowed by this model were produced with the hyperon in the backward hemisphere of the center of mass but <u>not</u> peripherally. Those reactions not allowed by a one-particle exchange model are consistent with isotropy in the center of mass.

One might also expect to see Σ (1385) production from the $\Lambda\bar{\Lambda}\,\pi^0$ final states. A scattergram of the $\Lambda\pi^0$ effective mass vs. the $\bar{\Lambda}\pi^0$ effective mass from the 40 observed events is shown in Figure 18. One notices some enhancement in the Σ (1385) region and an excess of events on the low mass side of this resonance region in both projections. The low mass effect is probably due to real $\Sigma^0\bar{\Sigma}^0$ events in which the two γ's fake a π^0 fit. This phenomenon was also noticed at 3.0 GeV/c along with similarly small resonance production.

One might also see Σ (1385) production in the $\Lambda\bar{\Lambda}\,\pi^+\pi^-$ and $\Lambda\bar{\Sigma}^0\,\pi^+\pi^-$+

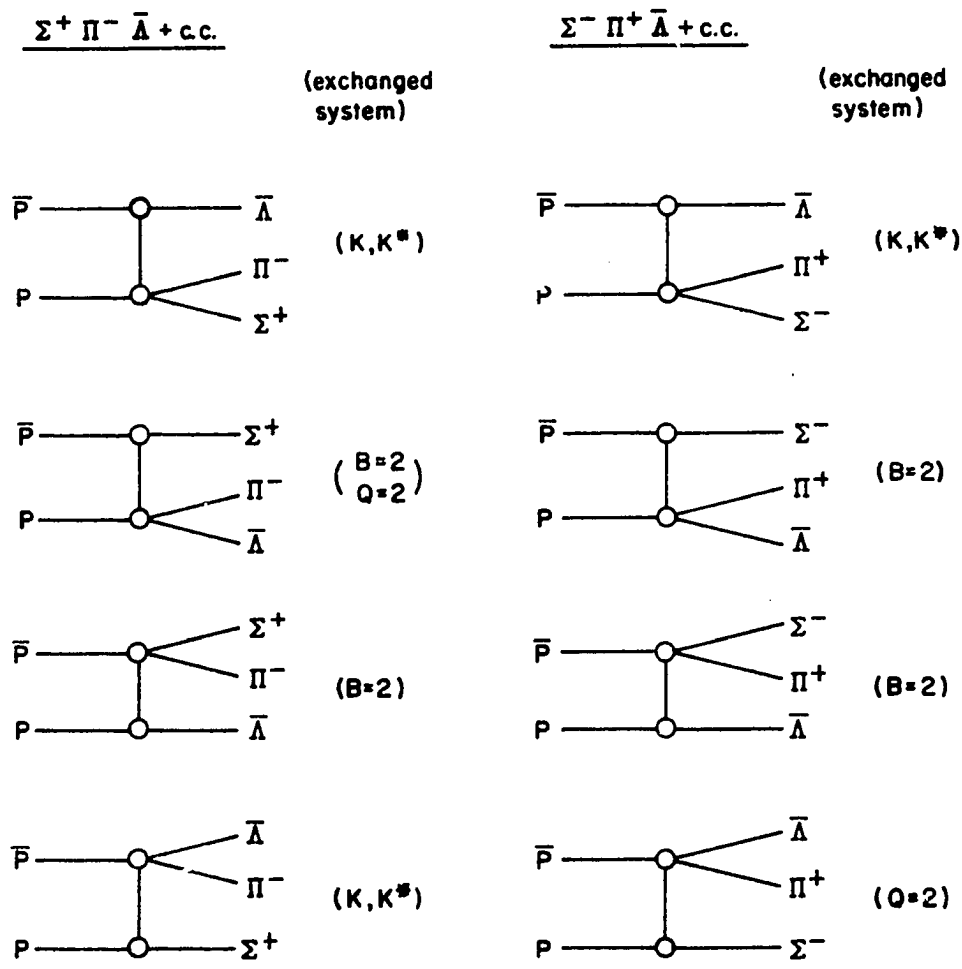

Figure 19. Possible exchange diagrams for the reaction's $\bar{p}p \rightarrow \bar{\Lambda}\Sigma^{+}\pi^{-}$ + c.c. and $\bar{p}p \rightarrow \bar{\Lambda}\,\Sigma^{-}\,\pi^{+}$ + c.c.

c.c. final states. However, since there were only five and three events respectively, the statistics were too limited to say anything meaningful.

VI. CONCLUSIONS

The cross sections for all hyper-antihyperon events observed in this experiment are given in Table IV. The $\Lambda\bar{\Lambda}$ and $\Lambda\bar{\Sigma}^{o}$ + c.c. cross sections are compared with those from other energies in Figure 5. It is of interest to note that, even though the threshold behavior of $\Lambda\bar{\Lambda}$ and $\Lambda\bar{\Sigma}^{o}$ + c.c. production is much different, they both approach $\sigma \approx$ 40 μb at high energy. The observed Λ-$\bar{\Lambda}$ mass difference at 2.4 and 2.9 GeV/c is .1 $\pm$ .4 and .6 $\pm$ .4 MeV/c^2 respectively. The mass difference is presented rather than the individual mass values as this cancels out any mass errors due to an inaccurately known magnetic field

There were three examples of $\Xi^{-}\bar{\Xi}^{-}$ production at 2.9 GeV/c (threshold is 2.6 GeV/c). These events, plotted with those found at 3.0, 3.25 and 3.7, show a tendency for the $\bar{\Xi}^{-}$ to be weakly aligned with the incident $\bar{p}$ (Figure 15).

The $\Lambda\bar{\Lambda}$ and $\Lambda\bar{\Sigma}^{o}$ + c.c. final states are observed to be highly peripheral indicating a t-channel exchange dominance. However a prediction for the differential cross section from a one meson exchange model with absorption, done for a slightly higher momenta (3.0 GeV/c) by Högaasen and Högaasen, is not as sharply peaked as the data. Both the single and joint spin-density matrix elements for the $\Lambda\bar{\Lambda}$ final state show an indication of t dependence, but with the limited statistics of this experiment the data is also consistent with no t dependence.

The 3-body final states are not produced as peripherally as the 2-body states. Those final states, which are consistent with t channel ex-

change of an observed particle (or system of particles) have angular distributions peaked forward but not strongly. Those states not consistent with the exchange of a known particle have an isotropic distribution. These final states also have lower cross sections. It is also interesting to note that in the $\Sigma^+\bar{\Lambda}\,\pi^-$ + c.c. final states there are three events where both the $\Sigma^+(\overline{\Sigma^+})$ and the $\bar{\Lambda}(\Lambda)$ are produced in the forward hemisphere.

Some $\Lambda(1520)$, $\Lambda(1404)$ and $\Sigma(1385)$ resonance production is observed in the $\Sigma^{\pm}\,\bar{\Lambda}\,\pi^{\mp}$ + c.c. events and some $\Sigma(1385)$ is observed in the $\Lambda\bar{\Lambda}\pi^0$ events.

VII. BIBLIOGRAPHY

1. N. Kwak, G. H. Mall, J. E. Manweiler, M. L. Nicholas, M. S. Redeker, T. A. Stringer, and R. Strump, Bulletin of the American Physical Society, New York Meeting, (Feb. 1969).

2. J. Badier, A. Bonnet, Ph. Briandet, and B. Sadoulet, Phys. Lett. 25B, 152 (1967).

3. G. P. Fisher, V. Domingo, A. J. Eide, J. Von Krogh, L. Marshall Libby, R. Sears, D. E. Bohning, W. J. Kernan, and L. S. Schroeder, Phys. Rev. 161, 1335 (1967).

4. B. Musgrave, G. Petmezas, L. Riddiford, R. Böck, E. Fett, B. R. French, J. B. Kinson, Ch. Peyrou, M. Szeptycka, J. Badier, M. Bazin, L. Blaskovic, B. Equer, J. Huc, S. R. Borenstein, S. J. Goldsack, D. H. Miller, J. Meyer, D. Revel, B. Tallini, and S. Zylberajch, Nuovo Cimento 35, 735 (1965).

5. C. Baltay, A Study of Antihyperon Production in Antiproton-Proton Reactions, Unpublished Ph.D. Thesis, Yale University, (1963).

6. C. Baltay, J. Sandweiss, H. D. Tazt, B. B. Culwick, J. K. Kopp, R. J. Louttit, R. P. Shutt, A. M. Thorndike, and M. S. Webster, Phys. Rev. 140, B 1027, (1965).

7. H. W. Atherton, L. M. Celnikier, B. R. French, J. B. Kinson, K. Myklebost, J. Pernegr, E. Quercigh, B. Sadoulet, Paper presented at the Lund International Conference on Elementary Particles, Lund, Sweden, June 1969, Department of Physics, The University of Kansas, Lawrence, Kansas.

8. C. Y. Chien, J. Lach, J. Sandweiss, H. D. Taft, N. Yeh, Y. Oren, and M. Webster, Phys. Rev. 152, 1171 (1966).

9. R. A. Jespersen, Two- and Three-Pion Production Without Annihilation in Antiproton-Proton Interactions at 2.4 and 2.9 GeV/c, Unpublished Ph.D. Thesis, Iowa State University, (1969).

10. J. P. Berge, F. T. Solmitz, and H. D. Taft, Rev. Sci. Instr. 32, 538 (1961).

11. W. J. Higby and A. H. Klein, U.S.A.E.C. Ames Laboratory On-Line Control System for Bubble Chamber Film Measuring, Report to be published, Department of Physics, Iowa State University, Ames, Iowa (ca. 1969).

12. W. J. Kernan, W. J. Higby, and I. H. Boessenroth, U.S.A.E.C. Report IS-1072 [Iowa State University, Ames, Iowa Institute for Atomic Research] (1964).

13. Particle Data Group, "Review of Particle Properties", UCRL-8030, Pt. 1 [California, Univ., Berkeley, Radiation Lab] (Jan. 1969).

14. U. Amaldi, T. Fazzini, G. Fidecaro, C. Ghesquiére, M. Legros, H. Steiner, Nuovo Cimento 34, 825 (1964).

15. H. D. D. Watson, Nuovo Cimento 29, 1338 (1963).

16. C. H. Chan, Phys. Rev. 133, B431, (1964).

17. H. D. D. Watson and J. H. R. Migneron, Phys. Lett. 19, 424 (1965).

18. H. Högaasen and J. Högaasen, Nuovo Cimento 40, 560 (1965).

19. N. Kwak, M. L. Nicholas, Paper presented at the Lund International Conference on Elementary Particles, Lund, Sweden, June 1969, Department of Physics, he University of Kansas, Lawrence, Kansas.

20. H. Pilkuhn and B. E. Y. Svensson, Nuovo Cimento 38, 518 (1965).

21. H. B. Crawley, Decay Angular Distributions and Decay Processes, Unpublished paper, Ames, Iowa, Iowa State University, Department of Physics, c.a. 1965.

22. K. Tanaka, Phys. Rev. 135, B1186 (1964).

VIII. ACKNOWLEDGMENTS

The author wishes to express his sincere appreciation to Professor W. J. Kernan for his guidance, advice and encouragement throughout the course of this investigation.

Thanks are also due to Dr. L. S. Schroeder for his many helpful suggestions, and to Dr. R. A. Leacock for his many useful discussions.

Much credit is also due to the programming staff headed by Mr. W. J. Higby and to the scanning and measuring staff directed by Mrs. Betty Pepper; without their work and assistance this investigation could never have been done.

The cooperation of the Iowa State Computing Center is also gratefully acknowledged.

Finally, the author wishes to thank his wife, Rosemary, for her understanding, support and encouragement throughout his graduate career.

IX. APPENDIX

The range of the missing mass from the reactions (1) $\bar{p}p \rightarrow (\bar{\Lambda})(\Sigma^o)$ or (2) $\bar{p}p \rightarrow (\Sigma^o)(\overline{\Sigma^o})$ when only the Λ is observed was calculated as follows:

$$E_{cm} = E_{\bar{\Lambda}(\overline{\Sigma^o})} + E_{\Sigma^o}$$

$$MM^2(\Lambda) = (E_{cm} - E_{\Lambda})^2 - (0 - P_{\Lambda})^2$$

$$= E_{cm}^2 - 2 E_{cm} E_{\Lambda} + M_{\Lambda}^2$$

where MM is the missing mass and all quantities are calculated in the center of mass.

		2.9 GeV/c	2.4 GeV/c
E_{cm}	=	2.76 GeV/c^2	2.55 GeV/c^2
For reaction 1			
$\lvert \vec{p}_{cm}(\Sigma^o) \rvert$	=	720 MeV/c	545 MeV/c
$E_{\Lambda_{max}}$	=	1365 MeV/c^2	1264 MeV/c^2
$E_{\Lambda_{min}}$	=	1274 MeV/c^2	1195 MeV/c^2
For reaction 2			
$\lvert \vec{p}_{cm}(\Sigma^o) \rvert$	=	675 MeV/c	480 MeV/c
$E_{\Lambda_{max}}$	=	1300 MeV/c^2	1235 MeV/c^2

$E_{\Lambda_{min}}$ = 1241 MeV/c^2 1166 MeV/c^2

Using these values we obtain:

$\bar{p}p \rightarrow (\bar{\Lambda})(\Sigma^o)$ with $\Sigma^o \rightarrow \Lambda(\gamma)$		$\bar{p}p \rightarrow (\bar{\Sigma^o})(\Sigma^o)$ with $\Sigma^o \rightarrow \Lambda(\gamma)$
$1152 \leq MM \leq 1352$	(2.9 GeV/c)	$1298 \leq MM \leq 1418$
$1145 \leq MM \leq 1290$	(2.4 GeV/c)	$1212 \leq MM \leq 1349$